**Master thesis**

# Ionisation and state preparation for single ion experiments

**Thomas Lafenthaler**

January 7, 2026

Supervisor: Thomas Monz
Co-Supervisor: Giovanni Cerchiari
Institut für Experimentalphysik

# Abstract

Trapped single ions provide an ideal platform for studying quantum optics, light-matter interactions, and quantum information processing. Many of these applications rely on the availability of well-defined and reproducible quantum emitters as well as precise control over the internal states of ions. To study both of these concepts, this thesis focuses on the isotope selectivity of neutral Barium (Ba) transitions as well as the state preparation of single trapped $^{138}\mathrm{Ba}^{+}$ ions.

The first part of this thesis introduces the theoretical framework for experiments, focusing on single $\mathrm{Ba}^{+}$ ions and light-matter interactions. Therefore, the working principle of Paul traps is presented, the Ba ion is introduced and fundamental light-matter interaction tightly related to the experiments and simulations presented in this work are established.

In the second part, the isotope selectivity of the neutral Ba $6\mathrm{s}^2\ {}^1\mathrm{S}_0 \rightarrow 6\mathrm{s}6\mathrm{p}\ {}^1\mathrm{P}_1$ transition at 553 nm is investigated and compared with the isotope selectivity of the $6\mathrm{s}^2\ {}^1\mathrm{S}_0 \rightarrow 5\mathrm{d}6\mathrm{p}\ {}^3\mathrm{D}_1$ transition at 413 nm. A secondary photon can be used in both cases to achieve isotope selective ionization of $\mathrm{Ba}^{+}$ ions. The isotope selectivity of the 553 nm transition was tested by carrying out spectroscopy and comparing the results with existing data. The isotope selectivity for other naturally available Ba isotopes is simulated for both transitions (553 nm and 413 nm) and for different angles between atomic beam and laser beam (90°, 85° and 80°). The simulations show, that under ideal conditions (when the atomic beam and ionization laser beam are orthogonal) both transitions perform similarly. However, the 553 nm transition exhibits greater robustness against Doppler shifts as the angle deviates from 90°. At an angle of 80° between the atomic beam and the laser beam, the maximum probability of generating $^{138}\mathrm{Ba}^{+}$ is 99 % using 553 nm, while the maximum probability of generating the isotope using 413 nm does not exceed 94 %.

In the third part of this thesis, we focus on state preparation of $\mathrm{Ba}^{+}$ ions in the $6\mathrm{P}_{1/2}$ state. A heralding state preparation scheme that exploits the spontaneous emission of a 389 nm photon during the decay of the excited state $6\mathrm{D}_{3/2}$ is introduced. The detection of a photon at this wavelength projects the ion into the desired state $6\mathrm{P}_{1/2}$ in a deterministic fashion. A simulation of this scheme shows that the preparation probability may exceed 78 %, and the heralding process ensures state preparation with 100 % fidelity, if a photon at a wavelength of 389 nm is detected. The state preparation method will be adopted in near-future experiments that are provided as an outlook at the end of this thesis.

# Contents

# 1 Introduction

Trapped atomic ions are a prominent systems for studying light-matter interactions and developing innovative quantum technologies [1–3]. The experiments with trapped ions shown in this thesis require two key technologies: ion traps to confine individual ions [4] and lasers to excite their internal electronic transitions [5]. Using these tools, ions are routinely cooled close to their motional ground state [6]. The work of this thesis contributes to this field of studies with two investigations: (a) isotope selective ionization of Barium (Ba) atoms via the $6s^2\ ^1S_0 \rightarrow 6s6p\ ^1P_1$ transition and (b) preparation of the rapidly decaying $6P_{1/2}$ excited state in $Ba^+$ via photon detection.

Isotope selective ionization of atoms is relevant for a number of scientific fields including studies of biomulecular building blocks in chemistry and biochemistry [7, 8], characterisation of the emission induced by combustion processes in environmental studies [9] or quantum computing and quantum optics applications in physics [10, 11]. In trapped ion experiments, isotope selective ionization provides the basis for isotope selective loading of ions. The letter enables the operation of quantum registers with identical qubits [12], to perform quantum optics experiments with identical emitters [13] and allows one to explore new physics with high precision spectroscopy [14]. Over the last decades a number of species were introduced for quantum information and optics experiments such as ions of Ytterbium [15], Beryllium [16], Strontium [17], and Calcium [18–20]. In this thesis' projects we worked with $Ba^+$ ions. Utilizing trapped $Ba^+$ ions for quantum optics experiments dates back to 1980 [21]. Over the past years, Ba has gained substantial interest in the community for the long lifetime of its excited $5D_{5/2}$ state of 30 s [22] and for the possibility to encode quantum information in its hyperfine states [23]. However, stable, non-zero-nuclear spin Ba isotopes have a natural abundance of 11.2 % for $^{137}Ba$ and 6.6 % for $^{135}Ba$. The zero-nuclear spin isotopes $^{138}Ba$, $^{136}Ba$ and $^{134}Ba$ are also naturally occurring with abundances of 71.7 %, 7.9 % and 2.4 %, respectively [24]. This implies that naturally occurring Ba has a more homogeneous isotopic distribution compared to other atoms like Strontium, with only three isotopes with a natural abundance above 1 % or Calcium, with only one isotope with a natural abundance above 1 % [25]. Thus it is relevant to implement efficient strategies to trap only one desired isotopic species.

In recent years, resonance enhanced multi-photon ionization (REMPI) schemes have been shown to offer significant advantages in isotope selectivity for Ba over other ionization techniques [26–29]. Historically, several transitions have been explored to achieve isotope selective ionization. For example, in 1988, the selectivity of neutral Ba was demonstrated using the $6s^2\ ^1S_0 \rightarrow 6s6p\ ^1P_1$ transition at 553 nm [30]. Shortly after, in 1992, the transition $6s^2\ ^1S_0 \rightarrow 6s5d\ ^1D_2$ at 413 nm was also shown to allow for isotope-specific ionization [31]. In addition, the use of a 791 nm laser was explored to excite neutral Ba from the $6s^2\ ^1S_0$ to the $6s6p\ ^3P_1$ state [32]. Building on these established methods, a 413 nm laser has been utilized in our laboratory for both the initial excitation and subsequent photo-detachment [33], leveraging the cost-effectiveness of employing a single laser source. However, the 413 nm transition of $^{138}Ba$ lies close to the respective transitions of $^{137}Ba$ and $^{135}Ba$, which are shifted by −43.7 MHz and 10.9 MHz, respectively. A recent article suggests that the $6s^2\ ^1S_0 \rightarrow 6s6p\ ^1P_1$ transition (553 nm) is more isotope selective with the smallest isotope shift ($^{137}Ba$) at 63.4 MHz [24].

A new ionization scheme was introduced to our laboratory during the course of this thesis exploiting the isotope selectivity of the 553 nm transition. It involves excitation to the $^1P_1$ state using a 553 nm photon, followed by ionization with a second photon at 416 nm. While this approach requires an additional laser compared to the REMPI scheme utilizing 413 nm light, the 416 nm laser is being implemented not only for ionization, but also for state preparation in $Ba^+$ ions. Its dual use justifies its integration into the setup.

This thesis focuses on state preparation through photon detection, a technique with potential applications in quantum networking and in the exploration of fundamental light-matter interactions. In our laboratory, we place a particular emphasis on spontaneous emission - a fundamental quantum phenomenon that occurs when an excited atom or ion returns to a lower energy state, emitting a photon in the process. Spontaneous emission is a common process in nature and plays a pivotal role in quantum optics research, and is tightly related to the lifetime of quantum states [34–36]. Our goal is to gain control over the spontaneous emission of $Ba^+$ ions via a hemispherical mirror that is used to retro-reflect the spontaneous emission of the ion on the ion itself. This capability allow us to suppress or enhance the rate of spontaneous emission depending on parameters such as the emitted photon's wavelength and the distance between the ion and the mirror's surface [37]. Control over spontaneous emission is advantageous for several reasons: First, it allows us to effectively extend the lifetimes of certain quantum states, which is beneficial for maintaining coherence in quantum information applications. Second, by modulating emission rates we can influence branching ratios and thus the probabilities that a photon will be emitted into particular state. Third, it can allow one to constrain the emission within a defined solid angle to suppress the measurement back-action [38].

In preparation for these experiments, we developed a technique to prepare a single $^{138}Ba^+$ ion in the $6P_{1/2}$ state. This state preparation scheme lays the foundation for controlling spontaneous emission and its potential applications. Conventional methods for preparing quantum states with high fidelity in quantum optics rely on optical pumping [39, 40] or direct excitation with laser pulses [41]. Unfortunately, the desired energy state $6P_{1/2}$ has a lifetime of 7.855(10) ns [39]. Therefore, to prepare the state via the transition from $6S_{1/2} \rightarrow 6P_{1/2}$, a short laser pulse is required in order to prevent the system from decaying while the state gets populated. For example in Ref. 41, a frequency-doubled Ti:sapphire laser with a pulse duration of $t_{\mathrm{pulse}} = 134(1)$ ps was used to excite Ytterbium ions from the ground to the $2P_{1/2}$ state. This state has a lifetime of 7.4(2) ns, which is comparable to the lifetime of the $6P_{1/2}$ state in $Ba^+$. We worked on an alternative approach that does not require such short pulses but relies on photon detection. We studied a heralded state preparation scheme exploiting the natural decay of the $6D_{3/2}$ into the $6P_{1/2}$ state in $Ba^+$. Through a projective measurement of the 389 nm photon emitted during this decay, the $6P_{1/2}$ state can be prepared with unitary fidelity as the preparation relies on the signal of photon detection. For that, we first pump the ions into the $6D_{3/2}$ state using three lasers at 1.7 µm, 614 nm and 416 nm. When a 389 nm photon is detected after the pumping process, it is guaranteed that the ion occupies the $6P_{1/2}$ state. In practice, we can exploit this detection-dependent state preparation scheme, by using correlation measurements between the emitted 389 nm photon and the respective secondary 493 nm or 650 nm photon.

The presented work is divided into the following main chapters:

- Chapter 2 provides a theoretical description of the physical concepts relevant to this thesis. The working principle of an ion trap is introduced. Then, the species used in the experiments, the $Ba^+$ ion, is described. Finally, key theories of light-matter interaction needed for the thesis are discussed, including dipole interaction, spontaneous emission, correlation functions, and resonance fluorescence spectroscopy.

- Chapter 3 describes the process of isotope-selective loading of single ions in a linear trap. The two-photon ionization scheme employed here uses a 553 nm photon for excitation followed by a 416 nm photon for electron detachment. A test chamber was set up to analyze the isotope selectivity of the 553 nm excitation beam via spectroscopy on the $6s^2\ ^1S_0 \rightarrow 6s6p\ ^1P_1$ transition. Additionally, simulations were carried out that shows the isotope selectivity for different Doppler broadenings.
- Chapter 4 proposes a heralding state preparation scheme for preparing $^{138}Ba^+$ ions in the $6P_{1/2}$ state. The ion is pumped into the $6D_{3/2}$ state using 1.7 µm, 614 nm, and 416 nm lasers. From the $6D_{3/2}$ state, the ion can spontaneously decay to the $6P_{1/2}$ state by emitting a 389 nm photon, which, when detected, projects the ion into the desired state. In the course of this thesis, a new detection setup including three new avalanche photodiodes (APDs) was built. The setup was tested by performing correlation measurements between an old fiber APD and the new free space APDs.
- Finally, the thesis concludes with an outlook for upcoming experiments. The focus lies on an experimental setup with a planar ring trap called the Panopticon apparatus. The chapter outlines how the heralded scheme for state preparation will be used in the setup to measure the branching ratio of the $6P_{1/2}$ state. These measurements will be performed in the presence of a boundary condition introduced by a hemispherical mirror. In this configuration, an emitted photon can interfere with itself - constructively or destructively - depending on its wavelength and the distance between the ion and the mirror. This interference effect allows for control over the branching ratio by tuning the mirror's radius.

# 2 Trapping $Ba^+$ ions and light-matter interaction

We focus on quantum optics experiments with single ions. For all of our experiments we need to store positively charged $Ba^+$ ions and control their internal energy structure. The following chapter starts with an introduction of Paul traps. After that, the $Ba^+$ ion will be introduced and its internal energy structure will be shown. Then, the light-matter interaction needed for this work is explained focusing on dipole interactions, spontaneous emission and correlation functions. At the end of the chapter a brief summary about resonance fluorescence spectroscopy will be presented.

## 2.1 Paul traps

One method for controlling single atomic ions at the quantum level is ion trapping. Trapping refers to confining individual particles, ideally in space at a distance from any experimental surface in order to minimize unwanted interactions with the environment. Part of the experiments that are presented in this thesis are performed using Paul traps, named after their inventor Wolfgang Paul [2, 4]. These traps confine ions in space via a combination of static and oscillating electric fields. The content of the following sections are based on 2 and 33, unless stated otherwise.

### 2.1.1 Working principle

The combination of static and oscillating electric fields of a Paul trap can be modeled by the following expression for the electric potential

$$\Phi(x,y,z,t) = U\frac{1}{2}\left(\alpha_x x^2 + \alpha_y y^2 + \alpha_z z^2\right) + \tilde{U}\cos(\Omega_{\mathrm{rf}}t)\frac{1}{2}\left(\alpha'_x x^2 + \alpha'_y y^2 + \alpha'_z z^2\right). \tag{2.1}$$

Here, $\Omega_{\mathrm{rf}}$ denotes the oscillating drive frequency and $\tilde{U}$ is the amplitude of the time-dependent sinusoidal oscillation. $t$ denotes the time, $U$ represents the applied DC voltage for the static part of the potential and $\alpha_i$ and $\alpha'_i$ with $i = (x,y,z)$ are geometric factors defined by the traps' geometry. Figure 2.1 depicts two Paul traps with different geometric factors. Paul traps aim at confining particles in free space, thus the electric potential needs to satisfy Laplace's equation $\Delta\Phi = 0$, which is the Poisson equation in absence of any charge density [42]. This imposes the following constraints on the geometric factors:

$$\alpha_x + \alpha_y + \alpha_z = 0$$

$$\alpha'_x + \alpha'_y + \alpha'_z = 0.$$

These constraints make it impossible to create a local minimum in the potential in all three spatial dimensions with a static field alone. Hence an oscillating field is required to create an effective potential with a local minimum in free space.

The motion of an ion confined in such a potential along a spatial dimension $i = (x, y, z)$ is described by the Mathieu equation [43]

$$\frac{d^2 r_i}{d\xi^2} + \left[a_i - 2q_i \cos(2\xi)\right] r_i = 0, \tag{2.2}$$

where

$$\xi = \frac{\Omega_{\mathrm{rf}} t}{2}, \quad a_i = \frac{4|e|\tilde{U}\alpha_i}{M{\Omega_{\mathrm{rf}}}^2}, \quad q_i = \frac{2|e|\tilde{U}\alpha_i'}{M{\Omega_{\mathrm{rf}}}^2}. \tag{2.3}$$

Here, M denotes the mass of the particle and the parameters $a_i$ and $q_i$ are known as stability parameters. The stability parameters are chosen to obtain the effective local minimum and confine a charged particle in space. In the context of quantum physics, these parameters are typically selected with the conditions $|a_i| \ll 1$ and $q_i^2 \ll 1$. Under these conditions, the trajectory of the ion in the potential can be approximated as

$$r_i(t) \propto \cos(\omega_i t)\left(1 - \frac{q_i}{2}\cos(\Omega_{\mathrm{rf}} t)\right), \tag{2.4}$$

where

$$\omega_i = \beta_i \frac{\Omega_{\mathrm{rf}}}{2} \tag{2.5}$$

and $\beta_i$ defined as

$$\beta_i = \sqrt{a_i + \frac{q_i^2}{2}}. \tag{2.6}$$

From Eq. (2.4), we see that the ion's motion can be separated into two components. One component oscillates at the frequency $\omega_i$ (where $\omega_i \ll \Omega_{\mathrm{rf}}$ for $\beta_i \ll 1$), known as secular motion. The rapid motion that oscillates with a reduced amplitude of $q_i/2$ at the drive frequency $\Omega_{\mathrm{rf}}$ is called micromotion. This motion is typically neglected. Under these conditions, the confinement of a single ion can be modelled by considering only the following pseudo-potential $\Psi$

$$\Psi = \frac{1}{2e} M \sum_i \omega_i^2 r_i^2. \tag{2.7}$$

### 2.1.2 The linear trap

In this thesis, I operated a linear Paul trap that already existed in the laboratory and helped assembling a planar ring trap that is set up by Yannick Weiser. In Fig. 2.1 both implementations are depicted. In the following I will focus on the linear trap (Fig. 2.1 a.)), which consists of four blade electrodes generating the RF field for radial confinement, and two endcap electrodes generating the static field for axial confinement. Each pair of opposing blades faces each other. The geometric factors in Eq. (2.1) are chosen to be

$$-(\alpha_x + \alpha_y) = \alpha_z > 0$$

and

$$\alpha_x' = -\alpha_y'$$

with

$$\alpha_z' = 0.$$

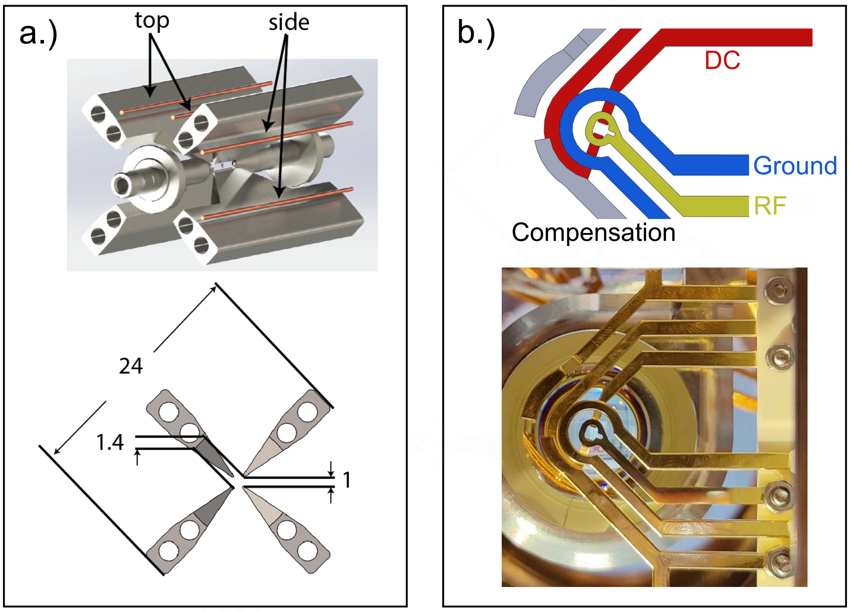

**Figure 2.1:** a.): Adapted from Ref. 44. An illustration of the dimensions of the linear quadrupole trap employed in this study. All distances are specified in millimeters (mm). The highlighted rods, located at the top and side, represent the electrodes utilized for micro-motion compensation. The distance between two opposite blades $2r_0$, as described in the text, measures 1.4 mm in this configuration. b.): A planar ring trap that is developed by Yannick Weiser. During the course of this thesis, I participated in building up the vacuum chamber for this apparatus, refered to as the Panopticon setup [45].

Here, the ion is confined in the $xy$ plane by a dynamic potential. Along the $z$ axis, a static electric field ensures axial confinement and closes the potential. With a distance of $2r_0$ between two facing rf electrodes, the oscillating part of the potential introduced in (2.1) simplifies to

$$\Phi(x,y,z,t) = \frac{\tilde{U}}{r_0^2}\cos(\Omega_{\mathrm{rf}}t)\left(x^2 - y^2\right). \tag{2.8}$$

The parameters for the trajectory of the ion motion are

$$q_x = -q_y = \frac{2|e|\tilde{U}_{\mathrm{rf}}}{M r_0^2 \Omega_{\mathrm{rf}}{}^2}, \quad q_z = 0$$

$$\beta_x = -\beta_y = \frac{q_x}{\sqrt{2}}, \quad \beta_z = 0$$

and the secular motion in the $xy$ plane can be written as

$$\omega_x = \omega_y = \frac{q_x \Omega_{\mathrm{rf}}}{2\sqrt{2}}.$$

In axial direction, the potential is confined by the applied voltage on the end-caps $U_{\mathrm{cap}}$, which leads to an axial motion that can be written as

$$\omega_z = \sqrt{\frac{2\kappa e U_{\mathrm{cap}}}{M z_0^2}}.$$

Here, $2z_0$ equals the distance between the two end-caps and $\kappa$ is a geometric factor that describes how the field penetrates at the trap center.

Particles are typically confined with a kinetic energy on the order of tens of meV, given by the environment [33]. In order to cool the ions motion further, laser cooling is used. For a detailed description of laser cooling see Ref. 20. I want to focus on so called Doppler cooling here, which works via momentum transfer during photon absorption. The cooling laser is red detuned with respect to the Doppler cooling transition. When the atom moves in the opposite direction of the wave vector $\vec{k}$, a photon can be absorbed due to the Doppler effect. This leads to a momentum transfer against the ion's direction of motion and thus slows down the particle. The photon emitted by spontaneous emission afterwards has a random direction, thus the net momentum transfer is zero. With this method, we are able to cool down the harmonic motion of the ion to its Doppler limit given by

$$T = \frac{\hbar\Gamma}{2k_B}, \tag{2.9}$$

where $\Gamma$ is the decay rate of the state used for the cooling process and $k_B$ the Boltzmann constant. For a quantum physics description of the ions motion, the creation ($\hat{a}_i^\dagger$) and annihilation ($\hat{a}_i$) operators are introduced [20]

$$\begin{aligned} \hat{a}_i^\dagger &= \sqrt{\frac{M\omega_i}{2\hbar}}\,\hat{r}_i + \frac{i}{\sqrt{2M\hbar\omega_i}}\,\hat{p}_i \\ \hat{a}_i &= \sqrt{\frac{M\omega_i}{2\hbar}}\,\hat{r}_i - \frac{i}{\sqrt{2M\hbar\omega_i}}\,\hat{p}_i, \end{aligned}$$

where $\hat{r}_i$ and $\hat{p}_i$ are the position and momentum operator respectively. With $\hat{n}_i$, the number operator of the oscillation in the trapping potential, the Hamiltonian of this system is described as

$$\begin{aligned} H &= \sum_i \left(\frac{\hat{p}_i^2}{2M} + \frac{1}{2}M\omega_i^2\hat{r}_i^2\right) = \sum_i \hbar\omega_i \left(\hat{a}_i^\dagger\hat{a}_i + \frac{1}{2}\right) \\ &= \sum_i \hbar\omega_i \left(\hat{n}_i + \frac{1}{2}\right). \end{aligned}$$

Thus the spread of the wave function of a Fock state $|n\rangle$ with a mean phonon number $\langle\hat{n}\rangle = n$ is given by

$$\sqrt{\langle n|\hat{r}_i^2|n\rangle} = \sqrt{\frac{\hbar}{2M\omega_i}}\sqrt{2n+1},$$

where $n = 0$ for the ground state. For a trapped Ba$^+$ ion with a secular frequency of $\omega_i/2\pi = 1\,\mathrm{MHz}$, the ground-state wave packet has a spatial extent of approximately 6 nm. For an excitation level of $n = 15$ , the wave packet expands to around 35 nm [33]. This spread remains three orders of magnitude smaller than the diameter of a tightly focused laser beam, which is about 31 µm for a lens with a focal length of 150 mm, a beam diameter at the lens of 3 mm and at a wavelength of 493 nm. Consequently, the light field can be considered spatially constant across the atom.

## 2.2 The Ba$^+$ ion

There are several ion species that are suitable for quantum optics and quantum information experiments, including Ytterbium [15], Beryllium [16], Strontium [17], and Calcium. The latter, has been frequently used in Innsbruck for a variety of quantum optics [46, 47] and quantum information [48–51] experiments. When selecting an ion species for quantum experiments, one must consider certain fundamental constraints. For instance, it is helpful that the energy states can be accessed using commercially available laser sources. Additionally, Hydrogen-like ions are particularly favorable for quantum experiments due to their simple energy structures, which make them easier to control compared to other atoms.
The electronic structure of $^{138}$Ba$^+$, focused on in this work, is analogous to that of Xenon, featuring an additional electron in the outer shell [52]. In Fig. 2.2 a.), the energy structure of $^{138}$Ba$^+$ is presented, highlighting the relevant electronic transitions pertinent to this thesis. The vacuum wavelength $\lambda$ for each transition, along with the corresponding decay rate $\Gamma$, is indicated. All depicted transitions can be excited using commercially available lasers.
For the purpose of Doppler cooling, the transition from $6S_{1/2}$ to $6P_{1/2}$ is employed using a 493 nm laser that is stabilized to a Tellurium reference line [53] and an optical reference cavity. Additionally, a 650 nm laser serves as a repumper to depopulate the $5D_{3/2}$ state. The laser is locked to a cavity that is stabilized by the 493 nm laser beam. The required transitions for Doppler cooling are illustrated in Fig. 2.2 b.).

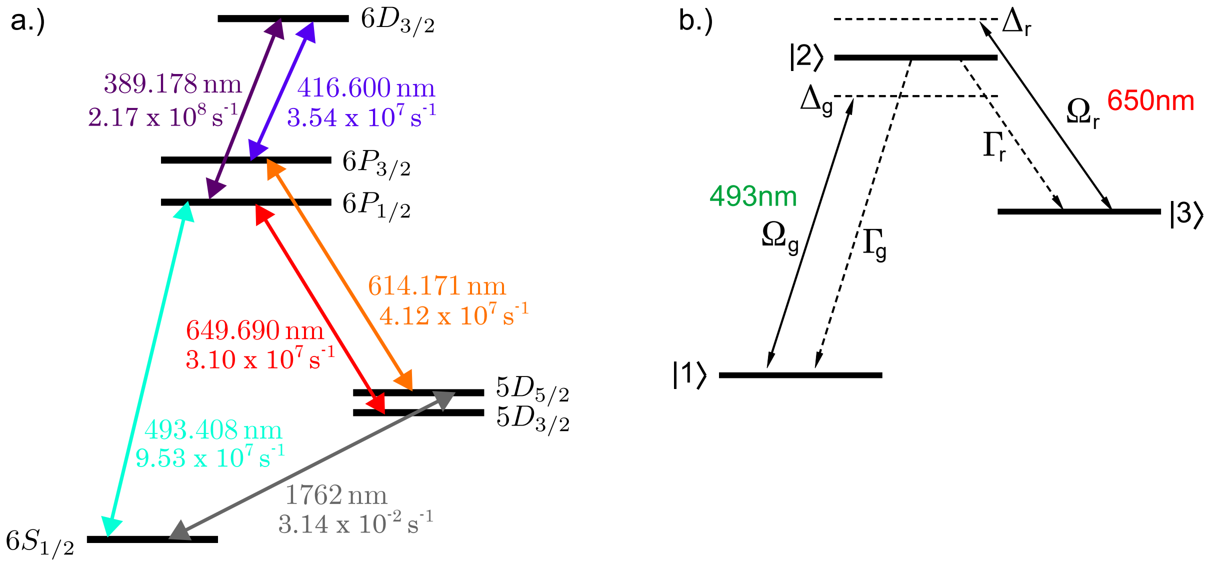

**Figure 2.2:** a.): The energy levels of $^{138}$Ba$^+$ relevant to this thesis are depicted, including all necessary transitions. The transitions between states are indicated in the corresponding colors of the emitted photons. For each transition, the decay rate $\Gamma$ in s$^{-1}$ (lower numbers) and the corresponding vacuum wavelength $\lambda$ (upper numbers) is provided [44, 54]. b.): Adapted from Ref. 33. The lower energy levels utilized for Doppler cooling in $^{138}$Ba$^+$ ions in the absence of a magnetic field. In the absence of a magnetic field, the system is characterized by three energy states. Here, $\Omega$ denotes the Rabi frequencies and $\Delta$ the detunings of the red (r) and green (g) lasers, respectively, while $\Gamma$ represents the decay rates of the corresponding transitions.

In our experimental setup, a magnetic field of about 4.45 G is applied to establish a quantization axis [55]. Consequently, we consider the splitting of states associated with angular momenta given by $\vec{J} = \vec{L} + \vec{S}$, where $\vec{L}$ denotes the orbital angular momentum and $\vec{S}$ the electron's spin. The application of a magnetic field results in $2J+1$ non-degenerate sublevels due to Zeeman splitting. Each Zeeman sublevel can be associated with a magnetic quantum number $m_j = -J, -J+1, \ldots, J-1, J$. The energy shift resulting from Zeeman splitting can be approximated for small magnetic fields as [56]

$$\Delta E_j = \mu_B m_j g_j |\vec{B}|, \tag{2.10}$$

where $\mu_B$ is the Bohr magneton and $g_j$ is the Landé factor. The Landé factor is calculated using the following expression [56]

$$g_j = g_L \frac{j(j+1)+l(l+1)-s(s+1)}{2j(j+1)} + g_S \frac{j(j+1)-l(l+1)-s(s+1)}{2j(j+1)}, \tag{2.11}$$

where $g_L = 1$ corresponds to the electron's orbital contribution, and $g_S \approx 2$ represents the gyromagnetic ratio. The principal quantum numbers of the corresponding angular momentum operators are denoted as s, j and l.

Considering that $^{138}\mathrm{Ba}^+$ has a single electron in the outer shell, the spin of the electron is $s = 1/2$, while the total orbital angular momentum $l$ takes values of 0, 1, and 2 for S, P, and D states, respectively. This results in a Landé factor of 2 for $6\mathrm{S}_{1/2}$, 2/3 for $6\mathrm{P}_{1/2}$, and 4/3 for $5\mathrm{D}_{3/2}$.

The absence of nuclear spin in $^{138}\mathrm{Ba}^+$ simplifies its energy structure, rendering it suitable for quantum optics experiments. However, for quantum information applications, the additional energy levels arising from hyperfine splitting can be exploited [23]. Ba has other isotopes with non zero nuclear magnetic moments such as $^{137}\mathrm{Ba}^+$ and $^{135}\mathrm{Ba}^+$ to use in future quantum information experiments.

**Table 2.1:** The different Ba isotopes, their natural abundance, and their isotope shifts in MHz relative to the $^{138}$Ba transition at 541 433 200 MHz (553 nm) [24, 57]. Odd isotopes have a non zero nuclear spin I and thus three excited states with different total angular momentum F. The isotope $^{133}$Ba is not included here, as it is not used in Innsbruck due to its radioactivity. Its handling would be subject to strict regulatory requirements, which makes its use in routine experiments impractical.

| **Isotope** | **Abundance** | **Isotope shift (MHz)** |
|---|---|---|
| 132 (I = 0) | 0.1% | 167.9 |
| 134 (I = 0) | 2.4% | 142.8 |
| 135 (I = 3/2) | 6.6% | 547.3 (F = 5/2)<br>326.7 (F = 3/2)<br>121.6 (F = 1/2) |
| 136 (I = 0) | 7.9% | 128.02 |
| 137 (I = 3/2) | 11.2% | 549.5 (F = 5/2)<br>274.6 (F = 3/2)<br>63.4 (F = 1/2) |
| 138 (I = 0) | 71.7% | 0 |

In Tab. 2.1 the different isotopes, their natural abundance and the isotope shift of the $6\mathrm{s}^2\ {}^1\mathrm{S}_0 \rightarrow 6\mathrm{s}6\mathrm{p}\ {}^1\mathrm{P}_1$ (553 nm) transition relative to $^{138}$Ba is shown. The downside of using Ba isotopes with non-zero nuclear spin for quantum information experiments is their low natural abundance compared to $^{138}$Ba. However the 6s$^2$ $^1$S$_0$ → 6s6p $^1$P$_1$ (553 nm) transition in neutral Ba is isotope selective. This allows us to use a REMPI scheme, with 553 nm as the resonant excitation step to isotope selectively ionize neutral Ba.

## 2.3 Light-Matter Interaction

Quantum optics investigates light-matter interactions at their most fundamental level, specifically the interaction between a single particle and a photon. This section delves into the interaction between a trapped ion and laser light. The main sources for the following chapters are [52, 56] and [33] unless stated otherwise. For clarity, we will examine the dynamics of a simplified three-level system such as that of $^{138}$Ba$^+$ in the absence of a magnetic field. Furthermore, we will assume that only the electric dipole moment of the atom interacts with the electromagnetic field generated by the laser. In the following sections, the ground state 6S$_{1/2}$ of $^{138}$Ba$^+$ equals $|1\rangle$, the 6P$_{1/2}$ state equals $|2\rangle$ and the 5D$_{3/2}$ state equals $|3\rangle$. Figure 2.2 b.) illustrates the notation employed in the subsequent sections.

### 2.3.1 Hamiltonian dynamics

One needs three terms to describe a system consisting of an atom and a light field: the Hamiltonian of the atom $\hat{H}_{\text{atom}}$, the Hamiltonian of the light field $\hat{H}_{\text{field}}$ and the Hamiltonian of the interaction between the atom and a laser field $\hat{H}_{\text{int}}$. However, the light field of a coherent light source with high photon numbers as utilized in our experiments can be approximated classically. Thus the Hamiltonian of the full system can be written as

$$\hat{H} = \hat{H}_{\text{atom}} + \hat{H}_{\text{int}}. \tag{2.12}$$

For a three-level system, the atomic Hamiltonian corresponds to

$$\hat{H}_{\text{atom}} = \sum_{a=1}^{3} |a\rangle\langle a| \hbar\omega_a, \tag{2.13}$$

where $\hbar\omega_a$ denotes the energy of the respective state. In the basis $a = 1{,}2{,}3$ with

$$|1\rangle = \begin{pmatrix} 1 \\ 0 \\ 0 \end{pmatrix}, |2\rangle = \begin{pmatrix} 0 \\ 1 \\ 0 \end{pmatrix}, |3\rangle = \begin{pmatrix} 0 \\ 0 \\ 1 \end{pmatrix}, \tag{2.14}$$

$\hat{H}_{\text{atom}}$ can be written as a matrix

$$\hat{H}_{\text{atom}} = \hbar \begin{pmatrix} \omega_1 & 0 & 0 \\ 0 & \omega_2 & 0 \\ 0 & 0 & \omega_3 \end{pmatrix}. \tag{2.15}$$

By choosing $|2\rangle$ to be at zero energy, the Hamiltonian can be rewritten as

$$\hat{H}_{\text{atom}} = \hbar \begin{pmatrix} \omega_1 - \omega_2 & 0 & 0 \\ 0 & 0 & 0 \\ 0 & 0 & \omega_3 - \omega_2 \end{pmatrix}. \tag{2.16}$$

The laser fields are coupled to the ion and drive the $|1\rangle \rightarrow |2\rangle$ and $|3\rangle \rightarrow |2\rangle$ transitions. These transitions occur at 493 nm and 650 nm respectively. The laser fields can be described by

$$\vec{E}_g(t) = \Re\left(E_{g0}e^{-i\omega_g t}\right) \cdot \vec{\epsilon}_g, \quad \vec{E}_r(t) = \Re\left(E_{r0}e^{-i\omega_r t}\right) \cdot \vec{\epsilon}_r, \tag{2.17}$$

where $g$ stands for green (493 nm) and $r$ for red (650 nm). Here, $\Re(z)$ is the real part of the complex number $z$. The amplitudes are denoted by $E_{g0}$ and $E_{r0}$, $\vec{\epsilon}_g$ and $\vec{\epsilon}_r$ denote the polarization and $\omega_g$ and $\omega_r$ represent the laser frequencies.

We assume that the size of the atom is much smaller than the wavelength of the light field, and thus the light field can be considered spatially constant across the atom. With this assumption, the light-matter interaction can be described simular to a dipole moment. Using this dipole approximation, the interaction Hamiltonian can be written as

$$\hat{H}_{\text{int}} = -\vec{D} \cdot \vec{E}, \tag{2.18}$$

where $\vec{D}$ denotes the atomic dipole operator.

State $|3\rangle$ is assumed to be stable because the transition between $|1\rangle$ and $|3\rangle$ is dipole forbidden, resulting in a long lifetime of about 30 s in Ba [54]. Thus, the atom-laser interaction can be expressed in terms of the coupling strength between the atom and the light field, represented by the Rabi frequencies $\Omega_{g,r}$

$$\hbar\Omega_g := \left(\vec{\epsilon_g} \cdot \vec{D}_g\right) \cdot E_{0g}, \quad \hbar\Omega_r := \left(\vec{\epsilon_r} \cdot \vec{D}_r\right) \cdot E_{0r}. \tag{2.19}$$

The Rabi frequency corresponds to a periodic variation of population in the excited state. With that, the interaction Hamiltonian $\hat{H}_{\text{int}}$ can be written as

$$\hat{H}_{\text{int}} = \hbar \begin{pmatrix} 0 & \frac{\Omega_g}{2}e^{+i\omega_g t} & 0 \\ \frac{\Omega_g}{2}e^{-i\omega_g t} & 0 & \frac{\Omega_r}{2}e^{-i\omega_r t} \\ 0 & \frac{\Omega_r}{2}e^{+i\omega_r t} & 0 \end{pmatrix}. \tag{2.20}$$

Combining both the interaction and the atomic Hamiltonian leads to

$$\hat{H} = \hbar \begin{pmatrix} \omega_1 - \omega_2 & \frac{\Omega_g}{2}e^{+i\omega_g t} & 0 \\ \frac{\Omega_g}{2}e^{-i\omega_g t} & 0 & \frac{\Omega_r}{2}e^{-i\omega_r t} \\ 0 & \frac{\Omega_r}{2}e^{+i\omega_r t} & \omega_3 - \omega_2 \end{pmatrix}. \tag{2.21}$$

To eliminate the explicit time dependence associated with the laser drives, we perform a unitary transformation into a rotating frame defined by the laser frequencies. The corresponding transformation matrix is

$$U = \begin{pmatrix} e^{-i\omega_g t} & 0 & 0 \\ 0 & 1 & 0 \\ 0 & 0 & e^{-i\omega_r t} \end{pmatrix}. \tag{2.22}$$

The Hamiltonian in a co-rotating frame using the unitary operator $U$ can be calculated via

$$\hat{H}' = U^\dagger \hat{H} U - i\hbar U^\dagger \frac{d}{dt} U. \tag{2.23}$$

With that and the laser detunings

$$\Delta_g = \omega_g - (\omega_2 - \omega_1), \quad \Delta_r = \omega_r - (\omega_2 - \omega_3), \tag{2.24}$$

the final Hamiltonian for the three-level system, including the coupling with the two laser fields, can be simplified to

$$\hat{H}' = \hbar \begin{pmatrix} \Delta_g & \frac{\Omega_g}{2} & 0 \\ \frac{\Omega_g}{2} & 0 & \frac{\Omega_r}{2} \\ 0 & \frac{\Omega_r}{2} & \Delta_r \end{pmatrix}. \tag{2.25}$$

### 2.3.2 Spontaneous Emission

Up to this point, no decoherence effects were considered. However, the 6P$_{1/2}$ or $|2\rangle$ state decays into a lower level state by photon emission with a lifetime of 7.855(10) ns [39]. Thus, we are no longer working with a pure state and need to describe the energy state via a density matrix $\hat{\rho}$ with Trace$(\hat{\rho}) = 1$. In the basis $a = 1,2,3$ introduced in the previous chapter, this density matrix can be written as

$$\hat{\rho} = \sum_{a,b=1,2,3} \rho_{a,b} |a\rangle\langle b|. \tag{2.26}$$

The diagonal elements of the matrix give the average populations in the corresponding state.
The dynamics of such a system can be described by the Master (Liouville) equation. Energy-dissipating phenomena, such as natural decay or laser spectral widths, are characterized by the system's interaction with the external environment, turning it into a non-isolated system. However, it can be demonstrated that the Master equation in Lindblad form describes such a system while preserving the trace of the density matrix. The Master equation can be written as

$$\frac{d\rho'}{dt} = -\frac{i}{\hbar} \left[\mathcal{H}', \rho'\right] + \gamma \mathcal{L}_{\text{damp}}(\rho), \tag{2.27}$$

where the Lindblad term $\mathcal{L}_{\text{damp}}$ describes an incoherent process that occurs with a rate $\gamma$ and is modeled with the collapse operator $\hat{C}_m$. The Lindblad term reads

$$\mathcal{L}_{\text{damp}}(\rho) = -\frac{1}{2} \left[\hat{C}_m^\dagger \hat{C}_m \rho + \rho \hat{C}_m^\dagger \hat{C}_m - 2\hat{C}_m \rho \hat{C}_m^\dagger\right]. \tag{2.28}$$

For spontaneous emission, the collapse operators are given by

$$\hat{C}_g = |1\rangle\langle 2|, \quad \hat{C}_r = |3\rangle\langle 2|, \tag{2.29}$$

and occurs with the respective decay rate $\Gamma_{r,g}$. The latter can be calculated via the dipole moment operator introduced before

$$\Gamma_{g,r} = \frac{\omega_0^3}{3\pi\epsilon_0 \hbar c^3} |\vec{D}_{g,r}|^2. \tag{2.30}$$

For the spectroscopy conducted in this thesis, a single 553 nm laser was used to excite neutral Ba from the ground state, 6s$^2$ $^1$S$_0$, to the excited state, 6s6p $^1$P$_1$. Additionally, only 553 nm fluorescence was detected during the experiment, corresponding to spontaneous emission from this excited state back to the ground state.
Under these conditions, population transfer to other atomic levels is negligible, because no other laser frequencies are present to drive transitions to higher or metastable states and only one natural decay path is present. Therefore, it is justified to approximate the atom as a closed two-level system, consisting of a ground state $|g\rangle$ and an excited state $|e\rangle$, in order to simplify the theoretical description and focus on the dominant dynamics observed in the experiment.
With that, the Master equation can be written as a set of four linear coupled equations, known as the optical Bloch equations:

$$\begin{aligned}
\frac{\partial}{\partial t}\hat{\rho}_{ee} &= -i\frac{\Omega}{2}\left(\hat{\rho}_{eg}-\hat{\rho}_{ge}\right)-\Gamma\rho_{ee},\\
\frac{\partial}{\partial t}\hat{\rho}_{gg} &= i\frac{\Omega}{2}\left(\hat{\rho}_{eg}-\hat{\rho}_{ge}\right)+\Gamma\rho_{ee},\\
\frac{\partial}{\partial t}\hat{\rho}_{ge} &= -\left(\frac{\Gamma}{2}+i\Delta\right)\hat{\rho}_{ge}-i\frac{\Omega}{2}\left(\hat{\rho}_{ee}-\hat{\rho}_{gg}\right),\\
\frac{\partial}{\partial t}\hat{\rho}_{eg} &= -\left(\frac{\Gamma}{2}-i\Delta\right)\hat{\rho}_{ge}+i\frac{\Omega}{2}\left(\hat{\rho}_{ee}-\hat{\rho}_{gg}\right).
\end{aligned} \tag{2.31}$$

Here, a perfect single-frequency laser ($\delta_l = 0$) is assumed.
With the so-called saturation parameter

$$s = \frac{2\Omega^2/\Gamma^2}{1+(2\Delta/\Gamma)^2}, \tag{2.32}$$

one can now calculate the density matrix in the case of a steady state for interaction times much longer than the decay rate. In these so-called steady-state solutions, the population of the excited state can be written independent of the initial atomic density matrix as

$$\hat{\rho}_{ee}(t\to\infty) = \frac{\Omega^2/\Gamma^2}{1+\left(\frac{2\Delta}{\Gamma}\right)^2+2\frac{\Omega^2}{\Gamma^2}} = \frac{s/2}{1+s}. \tag{2.33}$$

This equation corresponds to the absorption line shape of the atom, which indicates the steady-state probability of atomic excitation based on the Rabi frequency, natural decay rate, and the detuning of the driving field. Additionally, for a large saturation parameter, $\hat{\rho}_{ee}(t, s\to\infty) = 1/2$ holds, which is called saturation.
By defining a saturation intensity $I_{\text{sat}}$ as

$$I_{\text{sat}} = \frac{I\Gamma^2}{2\Omega^2}, \tag{2.34}$$

where $I$ is the intensity of the interacting light field, one can rewrite the steady-state solution as

$$\hat{\rho}_{ee}(t\to\infty) = \frac{1}{2}\frac{I/I_{\text{sat}}}{1+\left(\frac{2\Delta}{\Gamma}\right)^2+I/I_{\text{sat}}}. \tag{2.35}$$

This expression allows the distinction between two regimes. For high driving intensities $I \gg I_{\text{sat}}$, Eq. (2.33) can be simplified to a Lorentzian with FWHM $\sqrt{2}\Omega$

$$\hat{\rho}_{ee}(t\to\infty) \approx \frac{\Omega^2/4}{\Delta^2+\Omega^2/2}. \tag{2.36}$$

For weak driving intensities $I \ll I_{\text{sat}}$,

$$\hat{\rho}_{ee}(t\to\infty) \approx \frac{\Omega^2/4}{\Delta^2+\Gamma^2/2} \tag{2.37}$$

holds.
In resonance fluorescence spectroscopy, the frequency of the applied light field is tuned, and the fluorescence of the analyzed atom is detected. In this thesis, resonance fluorescence spectroscopy on neutral Ba was performed. Assuming a two-level system with the ground state $|g\rangle$, the excited

state $|e\rangle$, and a decay rate of $\Gamma_{eg}$, the total rate of photon emission $N_{\text{tot}}$ is proportional to the population of the excited state. Thus, $N_{\text{tot}}$ can be written as

$$N_{\text{tot}} = \Gamma_{eg}\rho_{ee}. \tag{2.38}$$

In the case of additional atomic decays $\Gamma_{\text{oth}}$, the total rate of photon emission becomes

$$N_{tot} = \Gamma_{eg}\rho_{ee} + \Gamma_{\text{oth}}\rho_{ee}. \tag{2.39}$$

In an experimental setup, an optical filter is used to detect the desired wavelength.

### 2.3.3 Correlation functions

In the course of this thesis, new free-space APDs were implemented. Correlation measurements between different APDs were conducted to ensure precise alignment on a single ion and test the functionality of the setup. The theoretical framework underlying these correlation measurements is presented in the following.

The properties of a propagating light field can be statistically described by a number of correlation functions of different moments. This thesis focuses on the first- and second-order correlation functions. The first-order correlation function characterizes the coherence of the light field. The second-order correlation function describes the probability of detecting a photon at time $t+\tau$ given that one was detected at time $t$. The first-order correlation function $g^{(1)}$ can be written as [58]

$$g^{(1)}\left(\mathbf{r}_1, t_1, \mathbf{r}_2, t_2\right) = \frac{\langle : E^*\left(\mathbf{r}_1, t_1\right) E\left(\mathbf{r}_2, t_2\right) : \rangle}{[\langle |E(\mathbf{r}_1, t_1)|^2\rangle \langle |E(\mathbf{r}_2, t_2)|^2\rangle]^{1/2}}, \tag{2.40}$$

where $E$ is the electric field depending on a point in space-time $(\mathbf{r}_i, t_i)$, $E^*$ is the complex conjugate, and "::" denotes time and normal ordering [33]. In the case where the fields are measured at the same point in space ($\mathbf{r}_1 = \mathbf{r}_2$) but at different times ($t_1 = t$, $t_2 = t+\tau$), the first-order function reduces to the form

$$g^{(1)}(t, t+\tau) = \frac{\langle : E^*(t)E(t+\tau) : \rangle}{\langle E^*(t)E(t)\rangle}. \tag{2.41}$$

The Fourier transform of Eq. (2.41) yields the spectral distribution of the corresponding light field

$$S(\omega) = \frac{1}{2\pi}\int_{-\infty}^{\infty} g^{(1)}(\tau)e^{i\omega\tau}\, d\tau. \tag{2.42}$$

Therefore, measuring the first-order correlation function $g^{(1)}(\tau)$ allows the spectral properties of the field to be determined.

The second-order correlation function $g^{(2)}$ can be written as [59]

$$g^{(2)}(t, t+\tau) = \frac{\langle : E^*(t)E^*(t+\tau)E(t+\tau)E(t) : \rangle}{\langle E^*(t)E(t)\rangle^2}. \tag{2.43}$$

Given that the intensity operator of a light field $I(t)$ is proportional to $E^*(t)\cdot E(t)$, this function is also called the intensity correlation function. In our experimental setup, we are able to measure intensity via APDs. These devices measure count rates $N$ of photons hitting their detection area.

In the following, a two-level system is assumed with a ground state $|g\rangle$ and an excited state $|e\rangle$. For single ion measurements, electric field operators $\hat{E}$ can be introduced to describe the correlation function [33]

$$\hat{E} = \xi e^{i\omega_l t} \sigma^-(t)\Theta(t), \tag{2.44}$$

with a constant amplitude $\xi$, the laser frequency $\omega_l$, and a step function $\Theta(t)$ with $\Theta(t < 0) = 0$ and $\Theta(t \geq 0) = 1$. The operator $\sigma^-(t) = |g\rangle\langle e|$ describes the atomic decay of the ion. This decay is associated with a photon emitted by the ion. In the our experiment, the Rabi frequency $\Omega$ of the driving field is much smaller then the decay rate $\Gamma$ of the excited state. Thus, the assumption is made that photons are elastically scattered. This means that the the atom stays in its initial energy level [60]. The correlation functions of first and second order can then be written in terms of the atomic operators

$$\begin{aligned} g^{(1)}(\tau) &= \frac{\langle : \sigma^+(t)\sigma^-(t+\tau) : \rangle}{\langle \sigma^+(t)\sigma^-(t) \rangle}, \\ g^{(2)}(\tau) &= \frac{\langle : \sigma^+(t)\sigma^+(t+\tau)\sigma^-(t+\tau)\sigma^-(t) : \rangle}{\langle \sigma^+(t)\sigma^-(t) \rangle^2}. \end{aligned} \tag{2.45}$$

For a laser-driven ion, we can use the Bloch equations for a fully quantitative description of the system. In the steady-state limit, the second-order correlation function can be reduced, using the quantum regression theorem [59], to

$$g^{(2)}(\tau) = \frac{\rho_{ee}(\tau)}{\rho_{ee}(\infty)}. \tag{2.46}$$

This means, that $g^{(2)}(\tau)$ can be expressed as the excited state population $\rho_{ee}(\tau)$ normalized by its steady-state limit $\rho_{ee}(\infty)$.

# 3 Isotope selective loading of single ions

Traditionally, we used two 413 nm photons for ionizing neutral Ba via a REMPI scheme utilizing the $6s^2\ {}^1S_0 \rightarrow 5d6p\ {}^3D_1$ transition in neutral Ba. During the course of this thesis, we exchanged the 413 nm laser with a 553 nm and a 416 nm laser utilizing the $6s^2\ {}^1S_0 \rightarrow 6s6p\ {}^1P_1$ transition. Additionally, a new oven mount was designed to be used for the recently installed Panopticon apparatus [45]. For testing both, the oven and the new ionization scheme, I build an ionization test chamber. In the following sections, the new ionization process is described. Then, the experimental setup, focusing on the ionization test chamber is introduced. The chamber made it possible to produce a spectrum of the first ionization laser that excited the neutral Ba from the $6s^2\ {}^1S_0$ state to the $6s6p\ {}^1P_1$ state. This spectrum is analysed and compared to already existing data. Based on the results, simulations were carried out to investigate the isotope selectivity of both the $6s^2\ {}^1S_0 \rightarrow 5d6p\ {}^3D_1$ (413 nm) and the $6s^2\ {}^1S_0 \rightarrow 6s6p\ {}^1P_1$ (553 nm) transitions, with particular focus on the robustness of the selectivity under the influence of Doppler broadening.

## 3.1 Two photon ionization process

To study interactions between a single ion and light, it is first necessary to prepare and trap individual ions in a controlled and reproducible manner. In the experiments I was involved in, this is achieved by generating ions from neutral atom sources, such as ablation targets or ovens, which supply neutral Ba atoms for subsequent ionization. Photo-ionization offers several advantages over electron impact ionization methods, including significantly improved loading efficiency (up to five orders of magnitude higher), isotope selectivity, and suppression of patch charging and stray field generation on the trap electrodes and surrounding mounts [33, 61, 62]. Additionally, photo-ionization allows for modifications, such as those implemented in this thesis, to be carried out without breaking the vacuum, as the ionization lasers can be mounted outside the chamber. In particular, the isotope selectivity of REMPI schemes, as described in [24], is especially beneficial in our laboratory, as Ba has several naturally abundant isotopes, four of which exceed 6.5 % abundance [24, 57]. This isotopic homogeneity makes it challenging to selectively trap a specific isotope without using isotope-selective ionization techniques. For quantum optics experiments with single ions, we primarily work with ${}^{138}$Ba, which has a natural abundance of approximately 71.7 % [24]. However, in one of our newer projects, we conduct quantum information processing experiments using Ba, where the information is meant to be stored in the hyperfine structure of the species. Since ${}^{138}$Ba lacks a nuclear spin and therefore has no hyperfine levels, we intend to use ${}^{137}$Ba for quantum computing experiments. In the following, different photo-ionization methods for ionizing Ba are introduced. Figure 3.1 illustrates the energy levels of neutral Ba, to help better grasp the involved processes [33].

In the past, we used two 413 nm photons to ionize neutral Ba atoms. The first photon excites the atom from the $6s^2\ {}^1S_0$ state to the $5d6p\ {}^3D_1$ via a quadrupole transition, while the second photon ionizes the species. This method of ionizing has the advantage of requiring only one laser source for both steps of the REMPI process. The transition we use to excite the neutral atom from the $6s^2\ {}^1S_0$ to the $6s6p\ {}^1P_1$ state (553 nm) has two significant advantage. First, it allows to separate the isotope selective excitation (first step) from the ionization (second step). This allows

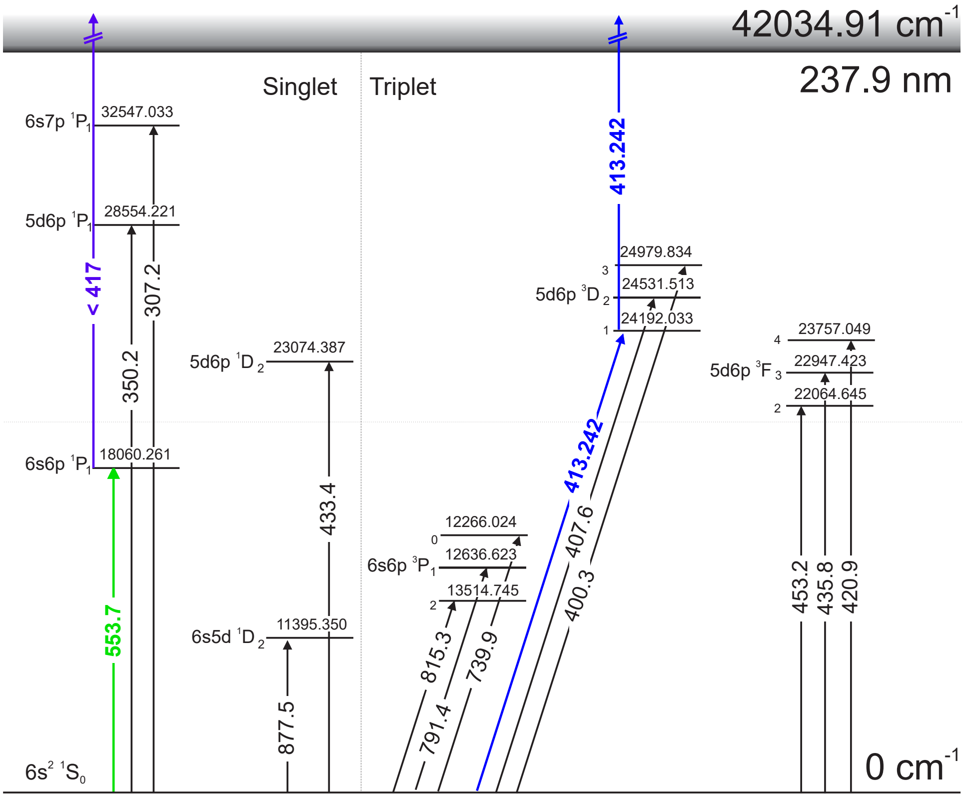

**Figure 3.1:** Adapted from Ref. 33. An excerpt of some of the energy levels in neutral $^{138}$Ba. The two ionization pathways utilized in our laboratory are highlighted. In earlier experiments, a resonance-enhanced multiphoton ionization (REMPI) scheme was employed, using the 6s$^2$ $^1$S$_0$ → 5d6p $^3$D$_1$ transition via 413 nm light. The ionization was completed when the excited atom absorbed a second 413 nm photon. In this thesis, ionization was achieved exploiting the 6s$^2$ $^1$S$_0$ → 6s6p $^1$P$_1$ transition using 553 nm light, followed by 416 nm light for REMPI.

us to use two different laser radiation fields that can be matched to avoid power broadening for selecting the isotope and retain efficient ionization. Secondly, the isotope shifts of the 553 nm transition with respect to $^{138}$Ba are all positive and significantly bigger then the isotope shifts of the 413 nm transition [24, 63]. This means the isotope selectivity of the 553 nm laser is expected to exceed the one of the 413 nm laser, especially if Doppler shifts are taken into account.

## 3.2 Isotope Selective Spectroscopy in a Neutral Ba Test Setup

The chamber described in the following, was developed with two primary goals: to test the performance of a neutral Ba oven, and to study the spectral properties of the 553 nm transition in neutral Ba. Previously, a similar oven failed to produce a detectable neutral atom beam. This failure was suspected to originate either from the oven itself or from the connection between the oven and its mount. To eliminate the latter as a potential source of error, a new oven mount was designed. The test chamber enables targeted and isolated testing of both components without interfering with the operation of larger experimental setups.

Beyond this diagnostic role, the chamber also enables spectroscopy of the 6s$^2$ $^1$S$_0$ → 6s6p $^1$P$_1$ transition at 553 nm. More recently, we have switched to a two-color ionization scheme involving a 553 nm and a 416 nm photon. However, for tuning the 553 nm laser to the frequency of the transition, we have relied on literature values taken from 24. In the referenced work, a Ba target is used as a source of neutral Ba to study isotope shifts, in contrast to the Ba oven employed in our experimental setups. Owing to these differences in the neutral atom source, the literature values cannot be applied directly and require experimental verification and fine tuning in our system. The chamber described in the following, therefore allows for a direct measurement of the transition frequencies and the corresponding isotope shifts, which are readily transferable to experiments in our laboratory.

One goal of this experiment is to verify that the 553 nm transition is indeed isotope selective and to compare the observed isotope shifts with previous publications. Furthermore, I simulate the ionization probability for different isotopes at various laser detunings and compare the results with the probability distribution from two-photon ionization using 413 nm light.

### 3.2.1 Setup

A custom-built oven mount was developed and tested in the ionization test chamber described in this section. This mount was designed to be compatible with the Panopticon experiment and was later installed there. For testing purposes, it was mounted on one of the flanges of the test chamber, equipped with electrical feedthroughs and positioned adjacent to the ablation target holders. Figure 3.2 shows the test chamber body in a.), the glowing oven with the fluorescent neutral atom beam in b.), CAD drawings of the oven and target mounts in c.), and a photograph of the installed components inside the Panopticon experiment in d.).

The oven used in the test was a commercially available resistively heated source (AlfaVacuo), consisting of a stainless steel tube preloaded with neutral Ba. The open side was initially sealed with indium to protect the material during storage and transport. This seal ruptures when the oven is first heated.

During the experiment, the oven was clamped into two electrically isolated parts of the custom mount. By applying currents between 4.5 A and 10 A through the stainless steel tube, the oven heats up via Joule heating [64], and neutral Ba atoms are released through the opened end.

Laser light at a wavelength of 553 nm was directed across the expected atomic beam, to confirm that the oven successfully emits neutral Ba atoms. The resulting fluorescence, caused by resonant excitation of the Ba atoms, was imaged using a camera. The emitted Ba atoms appear as a green tail in front of the oven's opening. An image of the fluorescence is shown in Fig. 3.2 b.). In this instance, the oven was operated at a current of 7.58 A, causing it to heat up and glow red.

For the spectroscopy of the $6s^2\ ^1S_0 \rightarrow 6s6p\ ^1P_1$ transition in neutral Ba using a 553 nm laser, it was crucial to align the laser beam perpendicular to the atomic beam from the oven to avoid distortions of the spectroscopy signal due to Doppler shifts. The laser entered the chamber through a viewport on the four-way cross and exited through the opposite viewport. During earlier tests, this exit viewport became partially coated with Ba, resulting in approximately 30 % of the laser light being reflected back into the chamber. This back-reflection was deliberately used during alignment: the laser was adjusted such that the incident and reflected beams overlapped, confirming perpendicular alignment with respect to the atomic beam and thereby improving the accuracy of the spectroscopy.

For the detection of fluorescence, an Andor Luca camera[1] was used. The camera was installed in front of one of the viewports on the six-way cross, with line of sight towards the oven's opening.

---

[1] Luca$^{\mathrm{EM}}$ R 604

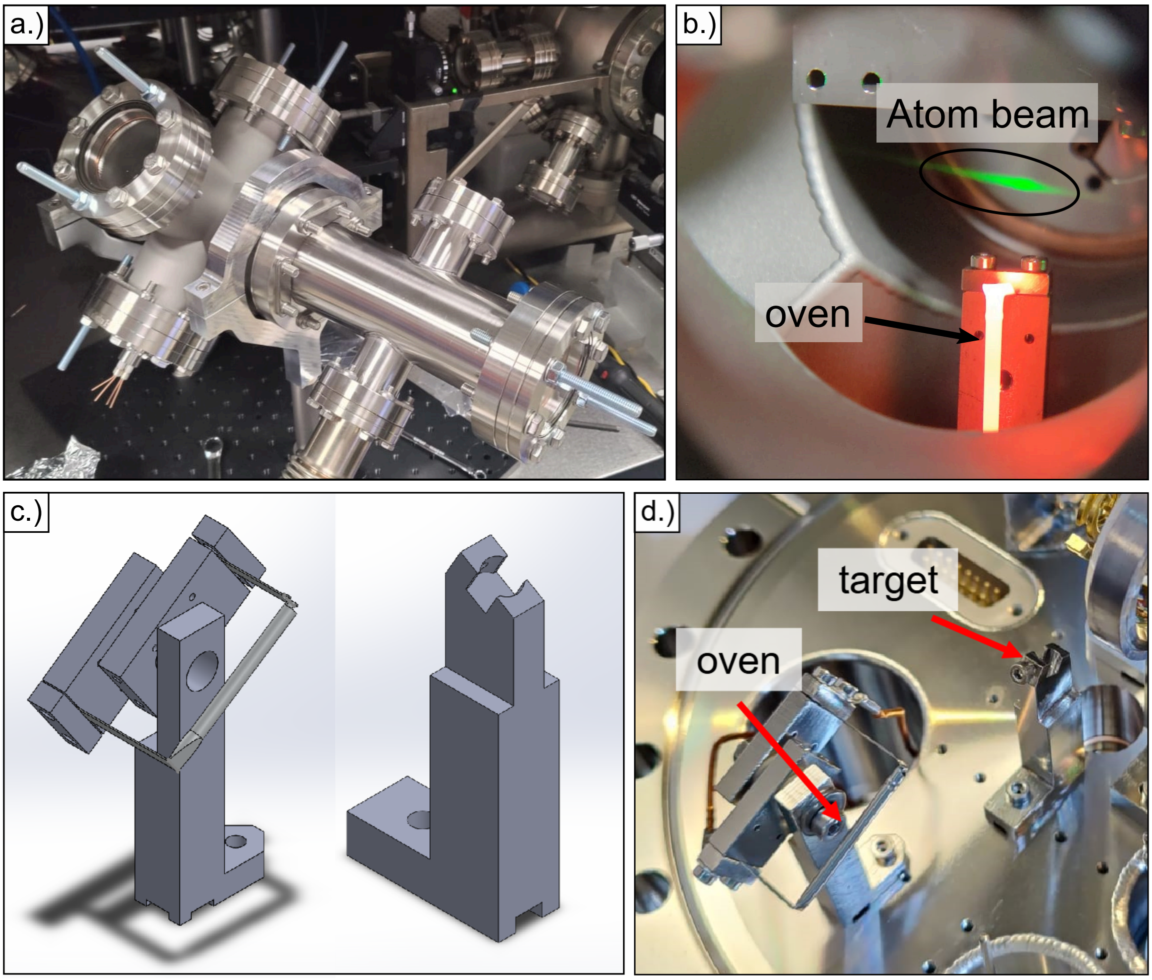

**Figure 3.2:** a.): The assembled vacuum vessel used for testing the Ba oven and for spectroscopy of the 553 nm transition in neutral Ba. The vessel comprises a six-way cross and a four-way cross, along with four viewports for optical access. It includes electrical feedthroughs for connecting the oven. b.): The powered Ba oven glowing red due to the applied electrical current of 7.58(1) A. The fluorescence of neutral Ba is visible as a green tail in front of the oven when a 553 nm laser at the transition frequency crosses the stream of neutral Ba. c.): The CAD drawings of the oven holder and the ablation target holder designed for the Panopticon apparatus. d.): A picture of the fabricated parts installed in the Panopticon setup.

Due to the black body radiation emitted by the oven, it was initially not possible to observe the fluorescence signal corresponding to the Ba atoms. However, by placing an 553 nm filter in front of the camera, the background light from the oven was removed, enabling the detection of the desired signal. A schematic drawing of the described setup is depicted in Fig. 3.3.
Due to the Doppler effect, two bright spots can be observed on the camera image, when the laser frequency is tuned away from the resonant frequency of the $6s^2\ ^1S_0 \rightarrow 6s6p\ ^1P_1$ transition. Figure 3.4 shows a sketch of the trajectory of a single atom as well as the cross section between the laser beams and the atom beam in order to explain this behaviour. Some of the atoms emitted by the oven are excited by the incident beam, while others are excited by the reflected beam coming back from the coated viewport. When the laser frequency is tuned away from the transition frequency, the velocity component of the particles in the direction of the laser must be taken into account. For particles moving opposite to the direction of the wave vector $\vec{k}$, the frequency of the

laser appears higher due to the Doppler shift, resulting in a blue shift of the transition frequency. Conversely, for particles moving in the direction of the wave vector $\vec{k}$, the transition frequency is shifted to the red. As a result, when the 553 nm laser is tuned off resonance, two bright spots instead of a single one become visible on the camera image. When the resonant frequency is approached, the distance between these two spots decreases until they merge.

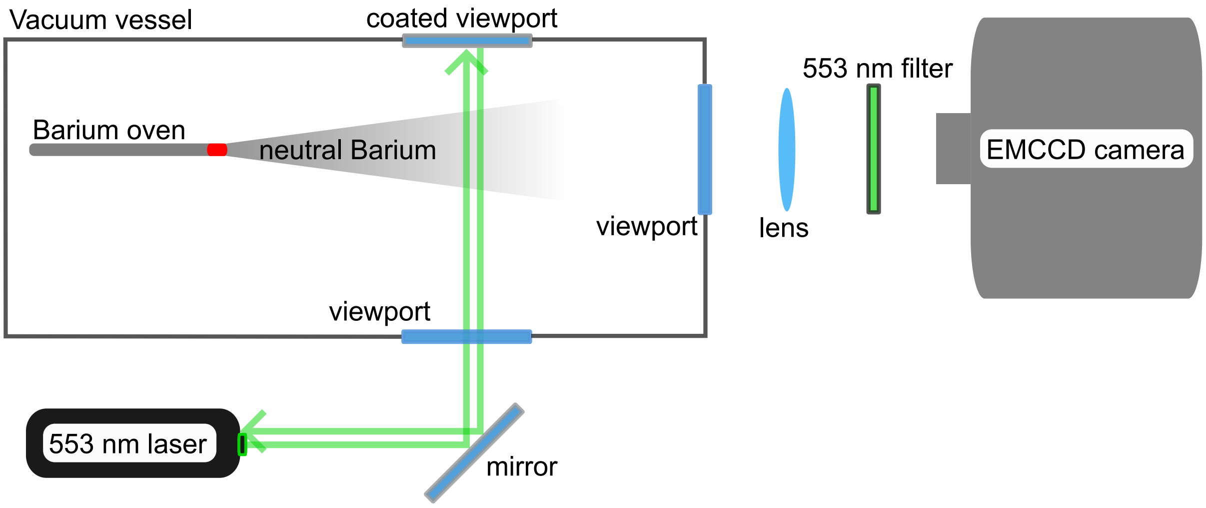

**Figure 3.3:** A sketch of the experimental setup. The vacuum vessel contains a Ba oven that emits neutral Ba atoms. A 553 nm laser is used to excite the neutral Ba beam, resulting in fluorescence. The photons emitted by the Ba atoms are detected by the detection setup on the right-hand side, which consists of a lens, a 553 nm optical filter, and an EMCCD camera. The 553 nm filter is necessary to suppress background radiation from the glowing Ba oven.

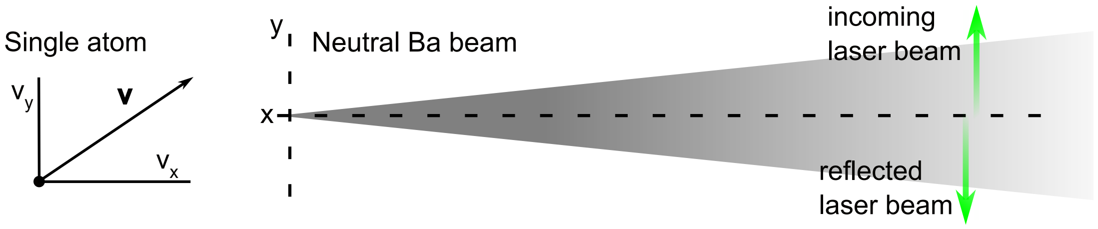

**Figure 3.4:** An illustration of the trajectory of a single ion alongside the cross-section of the interaction between the laser beams and the atomic beam. In this sketch, the laser is blue-detuned relative to the transition frequency. As a result, the incoming beam preferentially excites particles with a positive velocity component in the $y$ direction, while the reflected beam excites particles with a negative velocity component in the $y$ direction.

The camera was aligned by setting the frequency of the 553 nm laser such that only a single fluorescence peak appeared at the center of the image. Subsequently, the camera was rotated until the visible laser beam appeared horizontal. Afterward, the frequency of the 553 nm laser was scanned. A picture was taken by the camera every 0.5 s, and the corresponding 553 nm frequency was measured with a High-Finesse WS8 wavemeter. Additionally, the frequency of the 493 nm laser was measured to be used as a reference for the wavemeter drift. Fig. 3.5 shows the frequencies of the 553 nm and the 493 nm laser during the acquisition time.

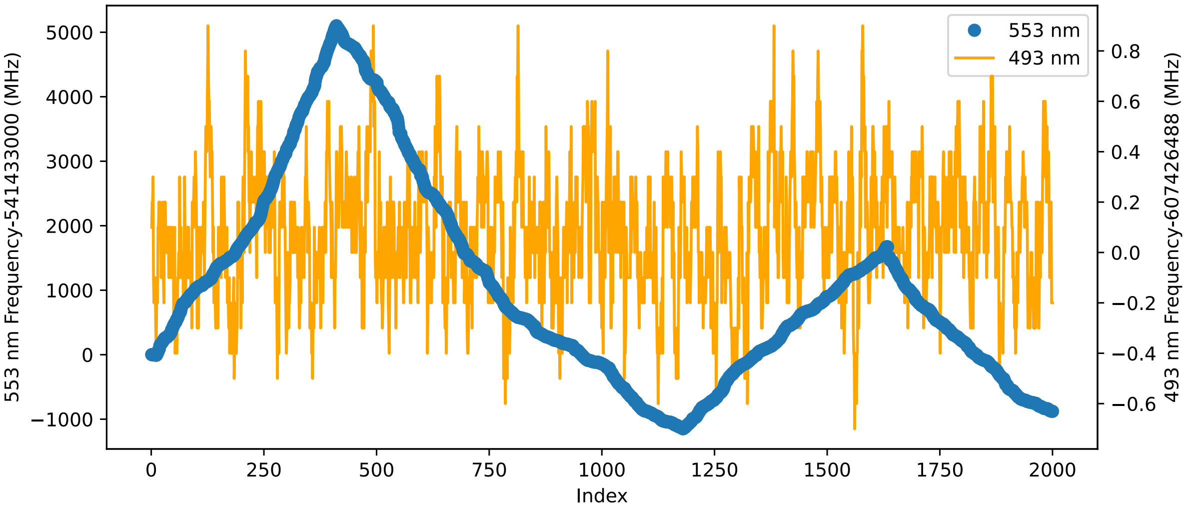

**Figure 3.5:** The frequencies measured during the acquisition time. The $x$ axis indicates the number of the measurement taken every 0.5 s. The blue curve shows the frequency of the 553 nm laser while the yellow curve shows the 493 nm laser frequency.

### 3.2.2 Preparation of Camera Images

One of the recorded images is shown in Fig. 3.6 a.). In the following chapter, the coordinate system indicated in the bottom left of this image is used. The recorded images were further processed to improve alignment accuracy beyond what was achievable during the experimental setup. One image, in which two bright spots resulting from the Doppler effect were clearly visible, was selected for this calibration. It was rotated from -90° to 90°, and for each angle, the image was projected onto the $y$ axis. The maximum intensity of each projection was plotted against the rotation angle. This analysis revealed a clear maximum between 0° and 1°, indicating that the laser beam was not perfectly horizontal in the original image. A second, finer scan within this range was performed, and a quadratic fit to the resulting peak values provided a more accurate estimate of the optimal rotation angle of 0.570(4)°. This is shown in Fig. 3.6 b.). All recorded images were then rotated accordingly for subsequent analysis.

The region of interest in the $y$ axis was determined by fitting a Gaussian curve to the projection onto the $y$ axis after applying the calculated rotation angle. The resulting fit is depicted in Fig. 3.6 c.). The region of interest on the $y$ axis was defined as the diameter of the Gaussian laser beam. Figure 3.6 d.) shows two pictures taken with the camera and cropped accordingly: one with the laser frequency resonant with the $6s^2\ {}^1S_0 \rightarrow 6s6p\ {}^1P_1$ transition, and one with the laser detuned from resonance.

The images were projected onto the $x$ axis. Images corresponding to frequencies from 541.428 000 THz to 541.431 500 THz and from 541.434 000 THz to 541.434 500 THz were averaged and subtracted from the data, to account for the background. These frequency intervals correspond to intervals in which no fluorescence light from the atoms was visible in the camera pictures. The resulting projection on the $x$ axis as a function of frequency is presented as a heatmap in Fig. 3.7 a.). Data points were included if the absolute value of the detected 553 nm frequencies minus 541.433 000 THz was less than 6000 MHz, and the absolute value of the detected 493 nm frequencies minus 607.426 488 THz was less than 1000 MHz. This filtering was performed to remove outliers due to the wavemeter. These outliers can be identified as data points, for which the

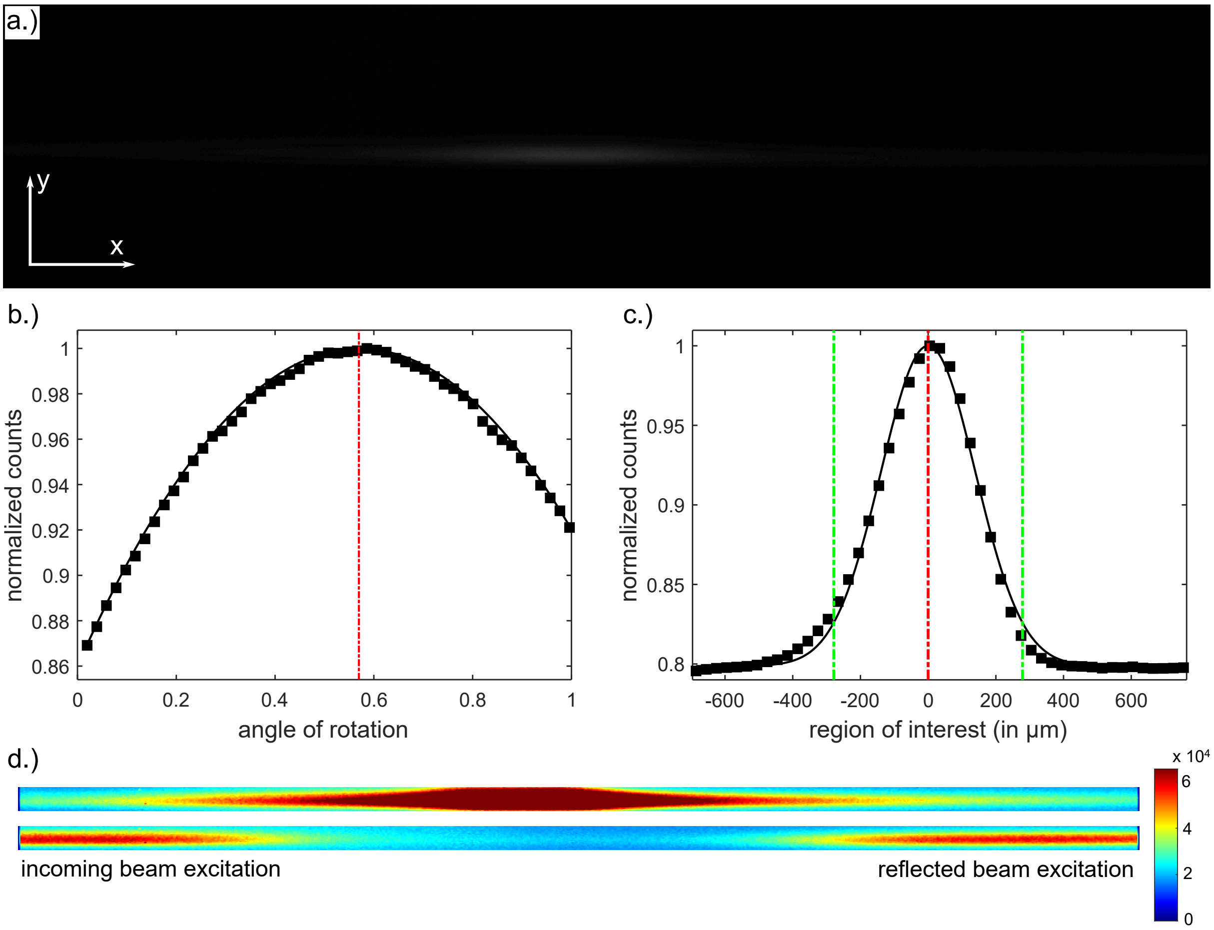

**Figure 3.6:** a.): An image taken with the EMCCD camera pre-processing. The image is not rotated and the region of interest on the $y$ axis is not defined. b.): For further processing, the pictures need to be rotated so that the wave vector $\vec{k}$ is parallel to the $x$ axis. To achieve this, one image was rotated between 0° and 1° and projected onto the $y$ axis. The maximum number of counts was plotted against the angle of rotation and a quadratic fit was applied. The maximum of this fit gives the angle of rotation used to rotate all of the taken images of 0.570(4)°. c.): One image with two dominant bright peaks was projected onto the $y$ axis, to define the region of interest on the $y$ axis. A Gaussian fit was applied to the data, identifying the peak (middle of the center of the laser beam, shown in red) and the upper and lower bounds (shown in green), defined as the peak plus and minus $\omega$. Here, $\omega$ is defined as the radius at which the fields amplitude falls to 1/e. d.): Processed camera images of the atoms fluorescence, when the laser frequency is on resonance (top) and tuned away from resonance (bottom). In the latter, two spots corresponding to the incoming and reflected laser beams are visible, exciting the atoms due to the Doppler shift. Both images are rotated and cropped accordingly. The colour in the plot denotes the number of counts.

wavemeter returned random floating numbers. The displayed wavelengths deviate significantly from the possible emission wavelengths of both the 493 nm and the 553 nm laser.

The next step involved determining the region of interest on the $x$ axis of the images. This was done by averaging the intensity values at the center of each image projection. A Gaussian curve was fitted to the projection onto the $x$ axis of the image with the highest average to identify the peak of the signal. Starting from the pixel where this peak was located, the intensities were plotted over the frequencies around the resonant frequency of the $^{138}$Ba transition. A second

Gaussian curve was fitted to this data to determine the full width at half maximum (FWHM) of this peak. This process was repeated 50 times, with each iteration expanding the region of interest by one pixel to the right and left of the previously selected area.
In the next step, the distance per pixel was determined by comparing two reference points in the camera image whose separation had been measured beforehand. This yielded a pixel size of approximately 30 µm. Using this calibration, the full width at half maximum (FWHM) of the transition frequency peak was evaluated as a function of the selected region of interest. This plot is shown in Fig. 3.7 b.). The graph demonstrates that the FWHM increases after approximately the 5th iteration. A region of interest of 10 pixels or 300 µm respectively was selected for the $x$ axis in the subsequent data analysis. The choice of 300 µm allowed for both, having a signal to noise ratio of about 350 and a resolution of 83 MHz, which allowed us to resolve all isotope. Besides, the typical trapping volume of an ion trap has lateral size in the same order of magnitude.

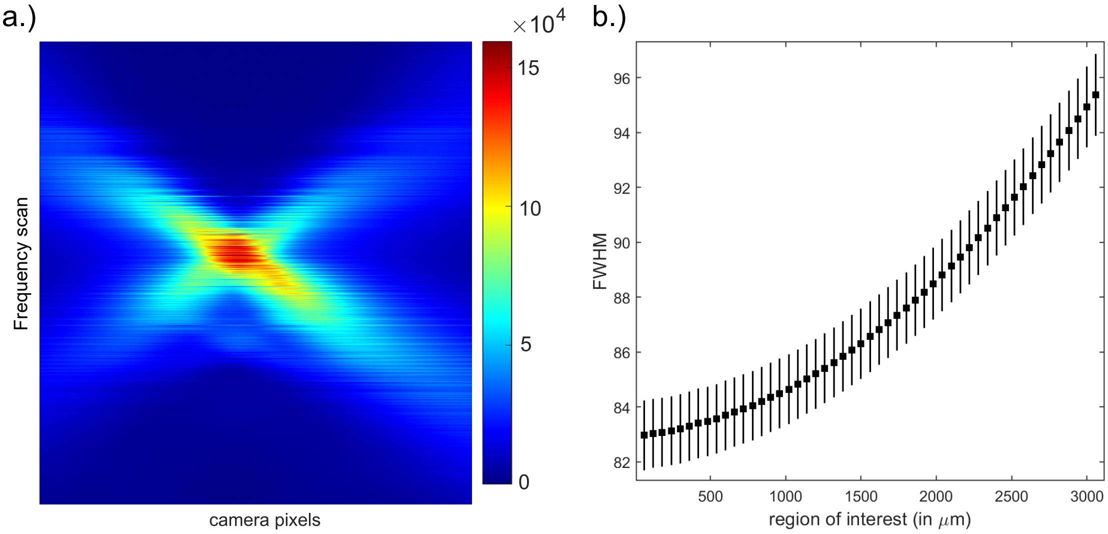

**Figure 3.7:** a.): Scanning of the 553 nm laser for the recorded datasets is visualized in this heatmap. Outliers are excluded, and only frequencies between 541.432 840 THz and 541.434 000 THz are considered. Each horizontal line of values in the heatmap corresponds to a projected image on the $x$ axis. The viewport opposite the one where the laser beam entered was coated with Ba, causing it to reflect part of the laser light. This reflection, combined with the Doppler effect, results in the characteristic X-shaped appearance of the heatmap. The colour indicates the number of counts in the plot. b.): The camera image with the highest intensity peak was used, to determine the region of interest on the $x$ axis. A Gaussian fit was applied to determine the center of the peak. From this center, the frequency against the detected intensity was plotted for a region of interest of one pixel. The resulting FWHM was calculated, and the process was repeated 50 times, each iteration including one additional pixel to the left and right of the previous region. The plot shows the FWHM of the transition frequency peaks against the region of interest in µm. The FWHM rises after approximately 300 µm, which is why this region of interest was used for the remainder of the data analysis.

As a result of this multi-step image processing, the experimental data were transformed into a consistent and well-defined spatial reference frame, with precisely aligned images and clearly selected regions of interest in both the $x$ and $y$ directions. In the $y$ direction, the region of interest was defined by the diameter of the laser beam, corresponding to 600 µm. In the $x$ direction, a region of 10 pixels, equivalent to approximately 300 µm selected. Background subtraction was performed by averaging images outside the resonance range and removing this background from the data. This preprocessing was essential for reliably extracting frequency-dependent fluorescence signals and enabling a quantitative analysis of the spectral profile of the atomic beam. With the background removed and the signal peak accurately localized, the dataset was prepared for further spectral evaluations, as presented in the following section.

### 3.2.3 Spectroscopy

The goal of this measurement was to resolve the isotope shifts of neutral Ba in the $6s^2\ ^1S_0 \rightarrow 6s6p\ ^1P_1$ transition at 553 nm using fluorescence spectroscopy. In particular, the goal was to identify spectral peaks corresponding to different naturally occurring Ba isotopes and compare their measured isotope shifts to known literature values.

For this purpose, the 553 nm laser was scanned across a frequency range covering the expected transitions of multiple isotopes. The resulting fluorescence signal from the atomic beam was recorded with a camera. A detailed calibration and correction procedure was implemented to account for background signals, image alignment, and wavemeter drifts. The processed data allowed the construction of a spectrum that resolved the individual isotope contributions.

With the background subtracted and the region of interest defined, wavemeter drifts were subsequently corrected to ensure frequency accuracy. During the frequency scan of the 553 nm laser, its wavelength was monitored using a High-Finesse WS8 wavemeter. Simultaneously, a second laser at 493 nm, already available in the laboratory and locked to a stable Tellurium transition, was also monitored. Since this reference laser exhibits negligible drift with respect to the atomic reference, it served as a basis for characterizing and correcting wavemeter fluctuations.

A built-in calibration function in the wavemeter software was employed, to quantify the wavemeter's drift behavior. This function allows the user to manually assign an absolute frequency to a chosen input channel. By deliberately assigning different frequency values to the stable 493 nm reference signal, the wavemeter adjusted its internal calibration accordingly. As a result, the displayed frequency of the 553 nm laser, measured on a separate channel, changed in response. This procedure was repeated for several artificially assigned values of the 493 nm frequency. The corresponding displayed values of the 553 nm frequency were recorded and plotted as a function of the assigned 493 nm values.

A linear fit was used to model the observed dependency between the 493 nm and the 553 nm frequency value displayed on the wavemeter. The slope of this fit, referred to as the calibration parameter $a$, was extracted. This parameter describes how changes in the reference frequency propagate to the measured values of the 553 nm laser due to wavemeter drifts. The respective data is shown in Fig. 3.8. The calibration parameter was then used, to correct the 553 nm frequency values. These corrected values were used in the subsequent data analysis to account for wavemeter drifts.

The resulting spectrum is shown in Fig. 3.9. In this measurement, an electron multiplier gain of 15 was set on the camera, and a current of 7.58(1) A was applied to the oven. The laser power for the incoming, collimated beam was measured to be 37.0(2) µW using a power meter. Four peaks are clearly visible and each peak observed can be attributed to one or more Ba isotopes. For clarity, all frequency values are given relative to the measured $^{138}$Ba transition at 541 433 184.98 MHz, corresponding to 0(4) MHz, with a full width at half maximum (FWHM) of 72.5(9) MHz. A smaller peak appears at 112(2) MHz with a FWHM of 104(7) MHz, which can be attributed primarily to $^{136}$Ba, but may also include contributions from other isotopes such as $^{135}$Ba and $^{137}$Ba and $^{138}$Ba. A broader peak at 284(14) MHz with a FWHM of 132(43) MHz likely originates from a transition associated with the odd isotope $^{137}$Ba. The fourth peak, centered at 525(54) MHz and exhibiting a FWHM of 232(138) MHz, is also attributed to this isotope with additional contributions from $^{135}$Ba. Due to their relatively low natural abundances and

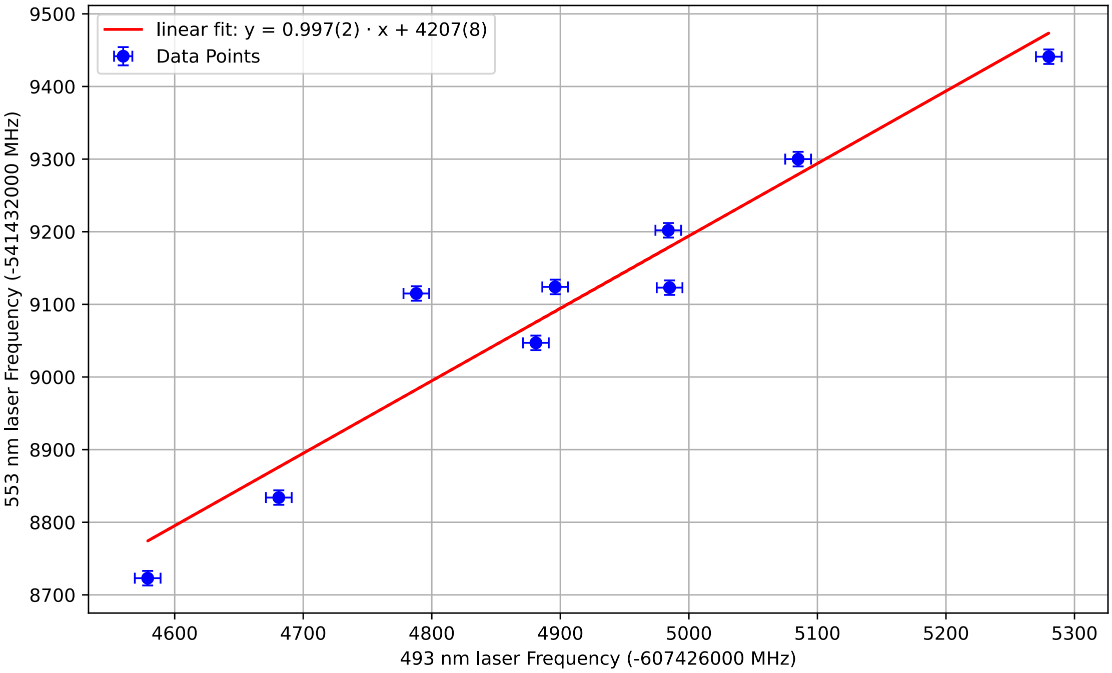

**Figure 3.8:** The frequency values manually assigned to the 493 nm wavemeter channel as a function of the corresponding displayed 553 nm frequencies, internally calibrated by the wavemeter. The slope of the linear fit depicted is used as the calibration parameter $a$. The error bars are determined by the internal statistical error of the wavemeter of 10 MHz.

hyperfine structure, these latter two peaks are less well resolved and exhibit larger uncertainties. Table 3.1 summarizes the Ba isotopes, their known isotope shifts relative to $^{138}$Ba as reported in [24, 57], and compares them with the results obtained from the present analysis. Thereby only isotopes are depicted, that could be assigned to a peak in the histogram. The measured isotope shifts are in agreement with values reported in the literature taking into account the statistical error of the measurement. The only measured isotope shift that does not agree with theoretical value is $^{136}$Ba. However, one has to keep in mind, that the respective $^{136}$Ba isotope with a natural abundance of 7.9 % is not the only species that could cause this peak. Additionally $^{135}$Ba (F=1/2) at 121.6 MHz, $^{137}$Ba (F=1/2) at 63.4 MHz and most importantly $^{138}$Ba at 0 MHz influence the position of the second peak in the spectrum. Therefore, the measured spectrum showing the isotope shifts in neutral Ba agrees with already existing values.

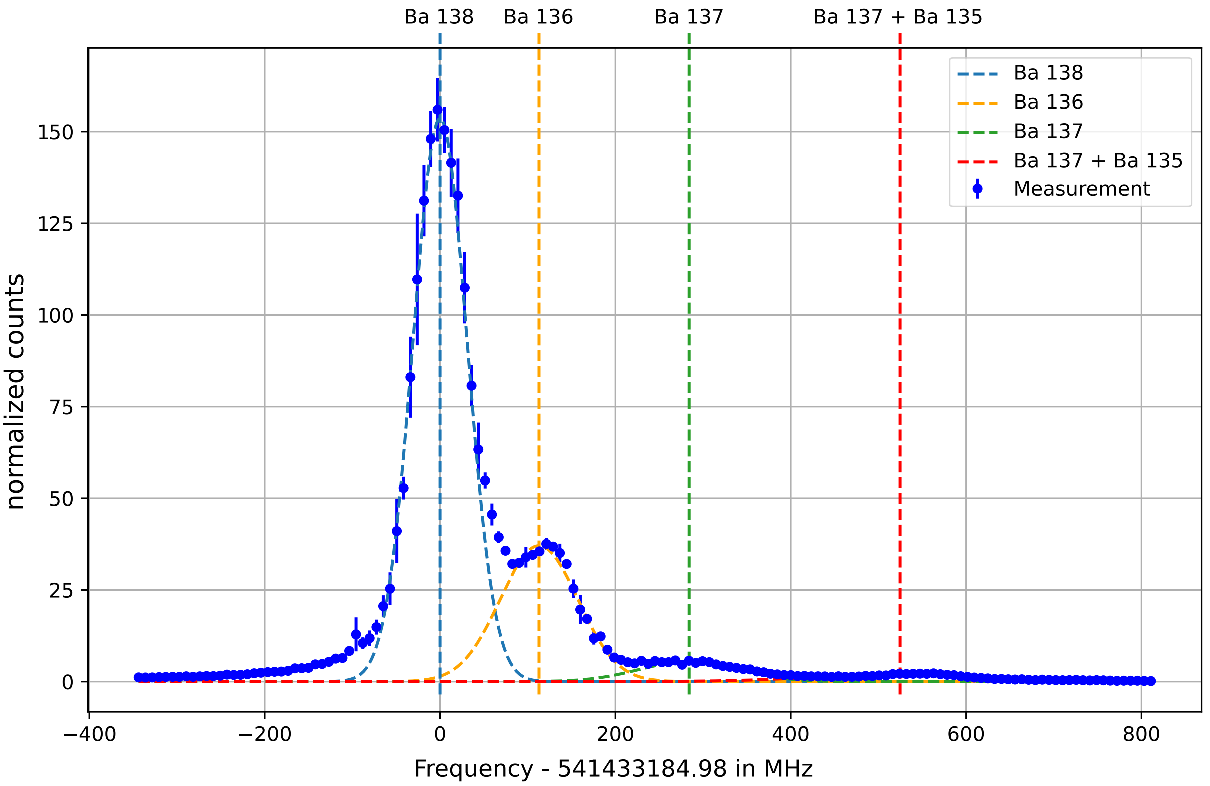

**Figure 3.9:** The measured intensity on an EMCCD camera while scanning the frequency of the 553 nm to identify different Ba isotopes. The dashed lines are fits used to determine the central frequency and the FWHM of the peaks. The first peak at a frequency of 0(4) MHz corresponding to $^{138}$Ba is particularly prominent. The second peak at 112(2) MHz can be assigned to $^{136}$Ba as well as other less common isotopes such as $^{132}$Ba, $^{134}$Ba, and $^{135}$Ba. The respective center frequencies of the peak at 284(14) MHz can be assigned to $^{137}$Ba as well as the peak at 525(54) MHz. The latter most likely also has also contributions of the $^{135}$Ba isotope.

**Table 3.1:** The different Ba isotopes, their natural abundance, and their isotope shifts in MHz relative to the $^{138}$Ba transition [24, 57]. Odd isotopes have a non zero nuclear spin I and thus three excited states with different total angular momentum F.

| **Isotope** | **Measurement (MHz)** | **Literature (MHz)** |
|---|---|---|
| 135 (I = 3/2) | 525(54) (F = 5/2) | 547.3 (F = 5/2) |
| 136 (I = 0) | 112(2) | 128.02 |
| 137 (I = 3/2) | 525(54) (F = 5/2)<br>284(14) (F = 3/2) | 549.5 (F = 5/2)<br>274.6 (F = 3/2) |
| 138 (I = 0) | 0(4) | 0 |

## 3.3 Trapping in the linear trap

With the spectroscopic characterization complete, the next goal is to load single $^{138}\text{Ba}^{+}$ ions into the ion trap. This requires several preparatory steps. First, the new 416 nm laser must be installed. Additionally, issues related to the alignment of the two photo-ionization (PI) lasers need to be resolved. Once these components are in place and properly aligned, the intensity and frequency of the 553 nm laser can be systematically optimized to establish the conditions most suitable for efficient and selective loading of single $^{138}\text{Ba}^{+}$ ions.

### 3.3.1 Installation and setup of the 416 nm laser

The laser light required for the second step of the REMPI scheme is provided by a Toptica DL100 Pro laser diode system. This laser was originally operated at a center wavelength of 422 nm and was modified by the manufacturer for operation at 416 nm. During the course of this master thesis, after about 6 months, the output power of the 416 nm laser decreased by roughly 50 %. For that reason, the grating of the laser needed to be realigned. Fig. 3.10 shows three curves where the optical output power L of the laser diode over the applied current I are depicted. Measurement 1 denotes the first dataset recorded upon receiving the laser diode. Measurement 2 corresponds to a state in which the internal grating of the diode was found to be misaligned, though the exact cause of the misalignment remains unknown. Measurement 3 was taken after the diode was realigned. The threshold current was measured to be 34.92 mA, 36.03 mA, and 38.92 mA respectively, at a diode temperature of 20 °C. While the threshold current increased slightly after realignment, the power-current characteristic became markedly steeper after the realignment of the grating. This results in higher output power beyond an applied current of approximately 42 mA, which is well below the typical operating point of around 90 mA. Therefore, the realigned grating offers enhanced performance within the standard operating range.

Fig. 3.11 presents a schematic of the laser's distribution board. The 416 nm laser setup is designed to provide light for photo-ionization in our experiments. The laser light is produced by a Toptica DL 100 pro laser diode, which passes through a half-wave plate (HWP) for polarization adjustment and is then directed to a polarizing beam splitter (PBS1) to split the beam into two parts.

The first part travels through a second HWP and polarizing beam splitter (PBS2) to allow power control. This beam is then coupled into a fiber via a mirror (M2) and a fiber collimator (FC1) and sent to the wavemeter for wavelength monitoring. This setup also provides an unused beamline for future experiments. The second part of the beam, after PBS1, is directed via mirror M1 to the three experimental setups available in our laboratory, namely the Panopticon setup, the Hyperion setup and the linear trap. Two flip mirrors (FM1 and FM2) control which experiment receives the beam. For the linear trap, the beam is coupled into a fiber via M3 and fiber collimator FC3. Upon exiting the fiber at the linear trap table through FC4, a third HWP cleans the polarization and controls the power sent into the double-pass setup.

The double-pass consists of two irises (I1, I2), two mirrors (M5, M6), two 150 mm focal length lenses (L1, L2), a quarter-wave plate (QWP), and an acousto-optical modulator (AOM). The QWP controls the power exiting the double-pass setup through PBS3, and the beam is then directed via mirrors M7 and M8 toward a dichroic mirror, where the second PI beam enters through FC5 and M9. Both beams are then sent to the linear trap.

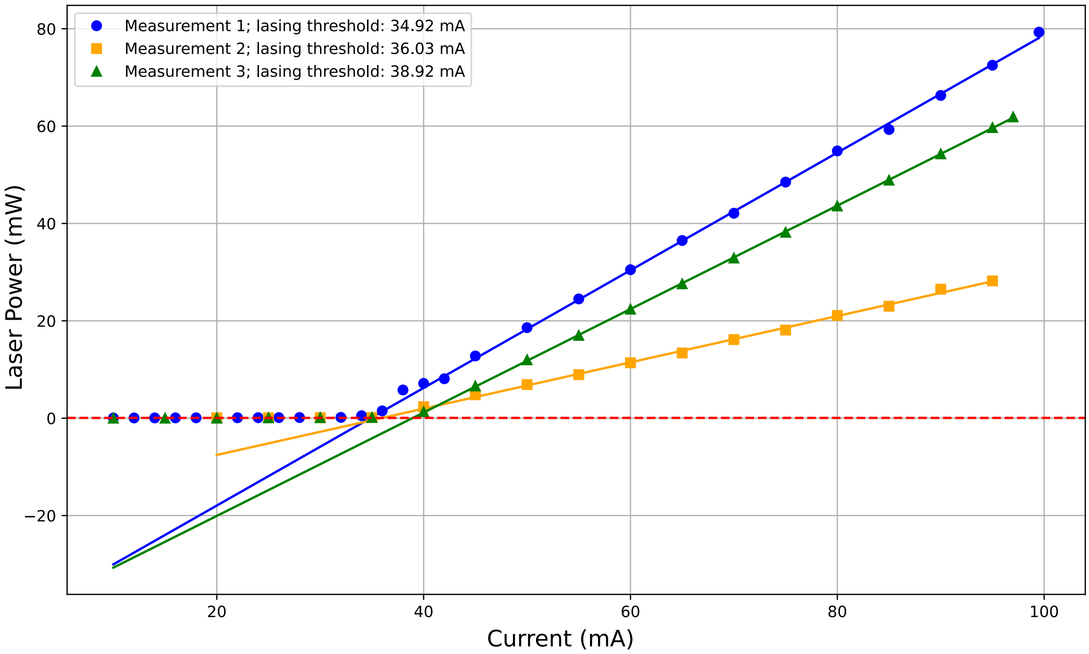

**Figure 3.10:** The optical output power L of the newly installed 416 nm laser diode as a function of the applied current I, operated at a temperature of 20 °C. The threshold current for the laser diode was 34.92 mA when we bought the diode, 36.03 mA after about half a year and 38.92 mA after realigning the grating. Although the threshold current increased slightly after the realignment, the slope efficiency of the laser improved significantly compared to measurement 2. As a result, the output power of the realigned laser diode surpasses that of the misaligned configuration beyond 42 mA. Since the laser is typically operated at around 90 mA, the realigned configuration provides superior performance in the regime of interest.

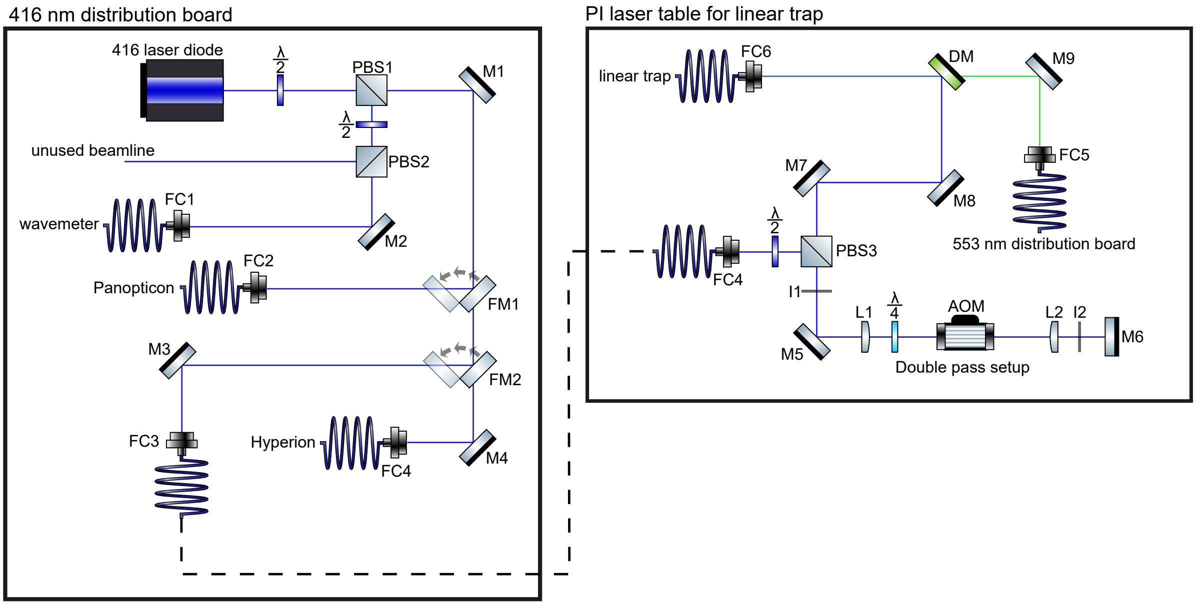

**Figure 3.11:** Schematic of the 416 nm laser setup. A Toptica DL 100 pro laser provides 416 nm light that passes through a half-wave plate (HWP) and is split by a polarizing beam splitter (PBS1). One part is directed through a second HWP and PBS (PBS2) for power control and is sent to the wavemeter via the fiber collimator 1 (FC1). The other part is directed to the experimental setups (Panopticon, Hyperion, and the linear trap). Flip mirrors (FM1, FM2) allow selection of the setup. The beam for the linear trap is coupled into a fiber via FC3, exits through FC4, and enters a double-pass setup. The double-pass consists of two irises (I1, I2), mirrors (M5, M6), lenses (L1, L2), a quarter-wave plate (QWP), and an acousto-optical modulator (AOM). After the double pass, the beam combines with the second PI beam at a dichroic mirror and is sent to the linear trap.

### 3.3.2 Alignment method of photo-ionization (PI) lasers

During trapping attempts in the linear trap, we observed that multiple ions appeared simultaneously on the camera image after a few minutes. This led to the conclusion that the ionization process of neutral atoms occurred in a different spatial region compared to the cooling process of the ions. Consequently, the potential energy of the trapped ions was too high for crystallizing and thus being visible. This issue was addressed by adjusting the alignment of the PI lasers to be co-linear with the cooling beams.

A practical solution was implemented based on the principle of counter-propagating beam alignment. The concept involves using an already aligned Doppler cooling beam - in this case, the 493 nm and 650 nm beams - that enters the vacuum chamber from one side and exits through the opposite viewport. A lens and mirror setup was then used to collimate the outgoing beam and couple it into a fiber collimator. By sending the PI beams through the same fiber in the reverse direction, they automatically propagate along the same path but in the opposite direction, thereby focusing at the same position as the Doppler cooling beams. This configuration ensures spatial overlap of the ionization and cooling processes. Additionally, the installed collimator serves as a stable reference point for aligning the Doppler cooling beams.

The described method was implemented by directing both PI beams (416 nm and 553 nm) through separate optical fibers on the optical table. The 416 nm beam was aligned through a double pass setup to allow frequency scanning for the heralding scheme introduced later in this thesis. Both beams were then combined using a dichroic mirror and coupled into a single fiber. The combined beam was directed into the trap chamber via a fiber collimator.

It was possible to trap a cloud of ions by spatially scanning the PI lasers. This allowed us to optimize the position of the Doppler cooling lasers using the camera. The 493 nm and 650 nm beams were scanned spatially to maximize the ions visibility. The outgoing cooling beams were then collimated and coupled into the collimator used for the PI beams, ensuring precise counter-propagation and overlap. The drawback of this setup is that the PI lasers now enter the vacuum chamber at an angle relative to the neutral Ba oven. This angle introduces a Doppler shift, which must be accounted for when selecting the frequency for the 553 nm beam.

### 3.3.3 Simulation: isotope selectivity

A numerical simulation was carried out to enable comparison between the newly introduced REMPI scheme using the 553 nm photon and the previously established scheme based on a 413 nm photon. The simulation presents the expected excitation probabilities for various isotopes as functions of laser frequency in the vicinity of the respective 553 nm and 413 nm transitions. Particular emphasis is placed on Doppler broadening effects resulting from different angles between the PI lasers and the neutral Ba atom beam. Isotope shifts and natural abundances were implemented as specified in Tab. 3.2, excluding $\mathrm{Ba}^{132}$ due to its low natural abundance of only 0.1 %.

The isotope peaks were modeled by sampling 1 million atoms in a Lorentzian with a FWHM of 18.9 MHz for the 553 nm transition and 9.15 MHz for the 413 nm transition in neutral Ba based on the values reported in [65] and [63], respectively. The thermal motion of atoms in the atomic beam was incorporated using a Maxwell-Boltzmann distribution. The velocity $v_{\text{laser}}$ of the individual atoms in the direction of the wave vector $\vec{k}$ can be given as a function of the angle $\theta$ between the atom flux and the incoming excitation beam as

$$v_{\text{laser}} = v \cdot \cos\theta. \tag{3.1}$$

**Table 3.2:** Each isotope included in the simulation described in the main text, along with its natural abundance and the isotope shifts (in MHz) for the $6s^2\ ^1S_0 \rightarrow 6s6p\ ^1P_1$ (553 nm) and $6s^2\ ^1S_0 \rightarrow 5d6p\ ^3D_1$ (413 nm) transitions, given relative to $^{138}$Ba. The values were take from [24] and [63] respectively.

| **Isotope** | **553 nm in MHz** | **413 nm in MHz** | **abundance** |
|---|---:|---:|---:|
| 138 | 0 | 0 | 0.717 |
| 137 (F = 5/2) | 549.5 | 651.4 | 0.112 |
| 137 (F = 3/2) | 274.6 | 223.5 | |
| 137 (F = 1/2) | 63.4 | -43.7 | |
| 136 | 128.02 | 178 | 0.079 |
| 135 (F = 5/2) | 547.3 | 633.3 | 0.066 |
| 135 (F = 3/2) | 326.7 | 248.8 | |
| 135 (F = 1/2) | 121.6 | 10.9 | |
| 134 | 142.8 | 124.2 | 0.024 |

The velocity $v$ was hereby sampled from 0 to $5v_{\text{peak}}$ with

$$v_{\text{peak}} = \sqrt{\frac{2k_bT}{m}}. \tag{3.2}$$

Here, T was chosen to be the temperature of the oven at 500 K and m=137.327 u is the mass of Ba [66].

Doppler broadening effects arising from the range of atomic velocities were modeled by calculating the convolution of the Lorentzian corresponding to the transition and the Gaussian corresponding to the Boltzmann distribution. The simulation was repeated for different angles $\theta$ between the atomic beam and the excitation laser. Each isotope's resulting spectral profile was scaled by its respective natural abundance. Fig. 3.12 shows the simulated excitation spectra as well as the excitation probabilities for three angles $\theta$ (90°, 85°, and 80°) using a.) 553 nm and b.) 413 nm laser light for ionisation. Excitation probabilities for each isotope were calculated separately for each angle by first summing the spectral profiles of all isotopes at a given angle. After that, the individual spectral profile of each isotope was divided by the sum over the spectral profiles.

Tab. 3.3 compares the ionization probabilities of the REMPI scheme using 553 nm light with the 413 nm method across the three simulated angles between ionization laser beam and atom beam (90°, 85°, and 80°) for all relevant isotopes. The following discussion focuses on the two most important isotopes for our experimental purposes: $^{138}$Ba, used in quantum optics, and $^{137}$Ba, used in quantum information experiments. For clarity, note that the frequencies mentioned below are offset by 541 433 200 MHz for the 553 nm data and 725 258 894.7 MHz for the 413 nm data to match the simulation plots in Fig. 3.12.

The simulation results indicate that the isotope selectivity of the 553 nm REMPI scheme at 90° is comparable to that of the 413 nm method. This is particularly relevant when targeting $^{137}$Ba, where the ionization probability at 90° reaches 94 % with 553 nm light, closely matching the 96 % achieved using 413 nm. However, the 553 nm method proves to be more robust against Doppler broadening. This becomes evident when considering not only the ionization probability but also the absolute number of ionized atoms. At 85°, for instance, the peak count for $^{137}$Ba using the

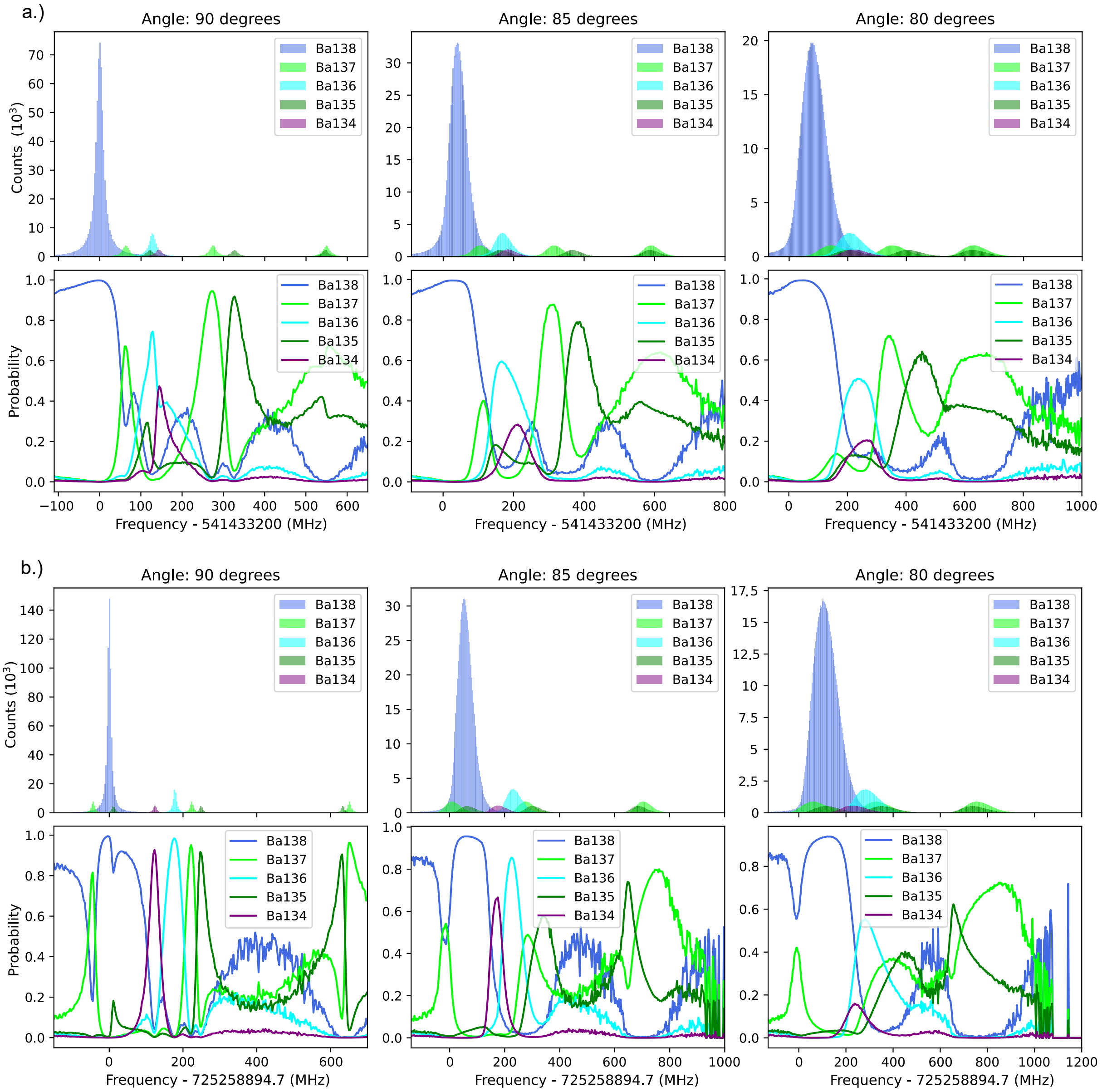

**Figure 3.12:** The simulation for the isotope selectivity of a.) the 553 nm transition (6s$^2$ $^1$S$_0$ → 6s6p $^1$P$_1$) and b.) the 413 nm transition (6s$^2$ $^1$S$_0$ → 5d6p $^3$D$_1$) in neutral Ba. A sample of 1 million particles according to a Maxwell-Boltzmann distribution was simulated. The transition width was chosen to be 18.9 MHz for the 553 nm transition and chosen to be 9.15 MHz for the 413 nm transition. The temperature of the oven was chosen to be 500 K for both. The angle between the atom flux and the laser beam is written on top of the graphs. The upper graphs show the number of excited atoms as a function of the laser frequency for each angle and isotope. The lower graphs determine the excitation probabilities for all isotopes at a certain laser frequency, which corresponds to the fraction of isotope species that will be trapped. The center frequencies for the simulations were taken from [24], [57] and [63].

413 nm method at 761.4 MHz is 277 with an excitation probability of 80 %. In contrast, the same simulation with 553 nm light yields 1727 counts at 315 MHz with an excitation probability of 88 %, using identical sampling conditions. This indicates that the 553 nm scheme provides a sixfold increase in the number of ions excited at the optimal frequency, which is a significant

improvement in both efficiency and robustness. A similar trend is observed for $^{138}$Ba. While this isotope is already efficiently ionized at 90° using either method, the 553 nm scheme consistently performs better across all angles. At 90° and 85°, the ionization probability exceeds 99.9 %. In contrast, the 413 nm method shows a reduction in performance with decreasing angle: dropping to 96 % at 85°, and further to 94 % at 80°. An additional advantage of using 553 nm photons for trapping single $^{138}$Ba$^{+}$ ions is the favorable isotope selectivity. Since all other Ba isotopes are excited at higher frequencies, the laser frequency can simply be tuned lower to increase selectivity for $^{138}$Ba. This approach does not work when using 413 nm light, as the $^{137}$Ba transition lies at a lower frequency than that of $^{138}$Ba. Repeated trapping attempts with different 553 nm laser powers and frequencies showed, that a laser frequency of 541 433 150 MHz and a power of approximately 10 µW yielded reliable trapping of single $^{138}$Ba$^{+}$ ions.

**Table 3.3:** The simulated maximum ionization probabilities for each isotope at three angles (90°, 85°, and 80°), comparing REMPI schemes using 553 nm and 413 nm laser light. The results indicate that while both methods perform similarly under ideal conditions (when the atomic and ionization beams are orthogonal) the 553 nm scheme exhibits greater robustness against Doppler shifts as the angle deviates from 90°.

| | **90°** | | **85°** | | **80°** | |
|---|---|---|---|---|---|---|
| **Isotope** | **553 nm** | **413 nm** | **553 nm** | **413 nm** | **553 nm** | **413 nm** |
| **138** | 100% | 99% | 100% | 96% | 99% | 94% |
| **137** | 94% | 96% | 88% | 80% | 72% | 72% |
| **136** | 74% | 98% | 60% | 86% | 51% | 55% |
| **135** | 92% | 92% | 79% | 74% | 64% | 62% |
| **134** | 47% | 93% | 28% | 67% | 20% | 16% |

# 4 State preparation of single ions

Part of the work in this thesis was devoted to developing a heralded technique for preparing the excited $6P_{1/2}$ state in $Ba^+$ ions. This technique potentially improves precision measurements of atomic properties such as branching ratios, lifetimes, and transition strengths. In particular, we are interested in measuring the branching ratio of the $6P_{1/2}$ state in $^{138}Ba^+$ in the presence of a boundary condition imposed by a hemispherical mirror. This topic will be discussed further in Sec. 4.4.

State-of-the-art experiments for measuring branching ratios in ions typically use sequences of optical pumping pulses and direct detection of emitted photons [39, 67]. However, such setups do not allow for the controlled preparation of an ion in the $6P_{1/2}$ state. Due to its lifetime of 7.855(10) ns [39], preparation of this state requires pulsed lasers with durations on the same order of magnitude, which is experimentally challenging. State preparation of states with similar lifetimes in Ytterbium were achieved by directly excite the ions to the $2P_{1/2}$ state utilizing a frequency-doubled mode-locked Ti:sapphire laser with a pulse duration of $t_{\text{pulse}}$ of 134(1) ps [41]. Achieving a comparable state preparation by directly exciting the $6P_{1/2}$ state with a pulsed 493 nm laser would require acquiring an additional dedicated laser system. Such an implementation would involve substantial financial cost and experimental effort. In contrast, the heralding scheme presented here relies exclusively on laser sources that are already available in our laboratory, making it the more practical approach.

The heralded state preparation technique proposed offers a solution by relying on the detection of a photon emitted during spontaneous decay from a higher-energy state, rather than using direct laser excitation from a lower-lying state [41]. The work on this heralded method performed as part of this thesis is presented in four parts: First, the heralded scheme is introduced to discuss its potential advantages over the direct-excitation techniques. Then, simulations of the technique are presented to show the optimal parameters suitable for experimental testing. Next, the current status of the experiment is presented with a measurement of the $g^{(2)}$ correlation function that was used to test the setup. Finally, an outlook is provided, presenting potential future applications of the state preparation scheme.

## 4.1 Heralding scheme: working principle

The key concept of the proposed state preparation scheme is to project the Ba ion into the $6P_{1/2}$ state by detecting the 389 nm photon emitted from the ion undergoing decay via the $6D_{3/2} \rightarrow 6P_{1/2}$ transition. This state preparation process can be described by two steps: (1) pumping and (2) measurement (or projection), which will be detailed in the following. The energy levels as well as the transitions needed for the state preparation scheme are visualized in Fig. 4.1.

For the state preparation scheme, we first populate the $6D_{3/2}$ state. This requires the usage of three laser pulses. Initially, a 1.7 µm laser is used to excite the $Ba^+$ ion to the $5D_{5/2}$ state. From there, a 614 nm and a 416 nm laser are needed to populate the $6D_{3/2}$ state. The $6P_{3/2}$ state acts as an intermediate state between the $5D_{5/2}$ and the $6D_{3/2}$ state. Figure 4.1 a.) depicts the energy levels and transitions needed for the pumping step of the state preparation scheme.

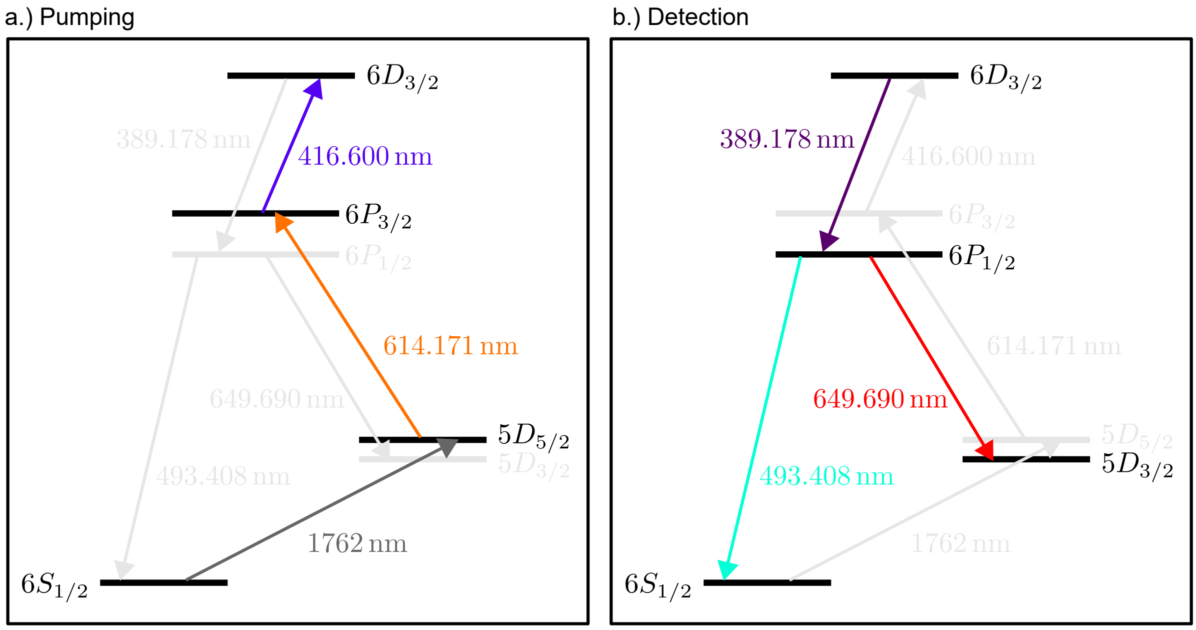
a.) Pumping

b.) Detection

**Figure 4.1:** The energy states required for the heralding scheme described in the main text. In a.), the pumping process is shown, where 1.7 µm, 614 nm, and 416 nm lasers are applied to populate the ion into the $6D_{3/2}$ state. In b.), the relevant transitions and energy levels for detection are depicted. When a 389 nm photon is detected, the ion has been projected into the $6P_{1/2}$ state. From there, either a 493 nm or 650 nm photon can be detected as the secondary emission.

Once the $6D_{3/2}$ state is populated, the ion will decay either to the $6P_{3/2}$ state by emitting a 416 nm photon or to the $6P_{1/2}$ state by emitting a 389 nm photon. The latter decay is more likely, with a branching ratio of about 1:5. Upon detecting a 389 nm photon, the ion is projected into the $6P_{1/2}$ state, completing the state preparation process. Correlation measurements can be performed between the 389 nm photon and the subsequent 493 nm or 650 nm photon. These correlation measurements should result in exponential decay curves, from which the branching ratio of the $6P_{1/2}$ state can be extracted. In Fig. 4.1 b.), the detection scheme is illustrated, showing the relevant transitions and energy levels involved in the process.
This detection method exploits the fact, that a 389 nm photon can only be detected, if the ion decays from the $6D_{3/2}$ state into the $6P_{1/2}$ state. That means in turn, that if a 389 nm photon is detected, that the ion is in the $6P_{1/2}$ state. This makes the proposed heralding scheme deterministic, while direct pulsed state preparation methods are probabilistic.

## 4.2 Simulation

The short lifetime of the $6P_{3/2}$ state (on the order of nanoseconds) makes it the primary loss channel in the proposed heralded state preparation scheme. Consequently, the strategy is to minimize the population in this state while transferring population to the $6D_{3/2}$ state as efficiently as possible. From there, approximately 80 % of the population decays via the emission of a 389 nm photon, resulting in population in the $6P_{1/2}$ state.
Three approaches were investigated to maximize 389 nm photon emission, and therefore the $6P_{1/2}$ population:

1. **Static case** – both the 416 nm and 614 nm pump lasers remain continuously on.
2. **Semi-static case** – the 416 nm laser is continuous, while the 614 nm laser is pulsed.
3. **Stimulated Raman Adiabatic Passage (STIRAP)** – both lasers are pulsed, with the 416 nm (Stokes) pulse preceding the 614 nm (pump) pulse.

The STIRAP timing is expected to suppress $6P_{3/2}$ population and thereby reduce loss [68].
The system dynamics were simulated using the basis

$$|0\rangle = \begin{pmatrix}1\\0\\0\\0\\0\\0\end{pmatrix}, |1\rangle = \begin{pmatrix}0\\1\\0\\0\\0\\0\end{pmatrix}, |2\rangle = \begin{pmatrix}0\\0\\1\\0\\0\\0\end{pmatrix}, |3\rangle = \begin{pmatrix}0\\0\\0\\1\\0\\0\end{pmatrix}, |4\rangle = \begin{pmatrix}0\\0\\0\\0\\1\\0\end{pmatrix}, |5\rangle = \begin{pmatrix}0\\0\\0\\0\\0\\1\end{pmatrix}, \tag{4.1}$$

where $6S_{1/2} = |0\rangle$, $6D_{3/2} = |1\rangle$, $5D_{5/2} = |2\rangle$, $6P_{1/2} = |3\rangle$, $6P_{3/2} = |4\rangle$ and $6D_{3/2} = |0\rangle$. In the rotating wave approximation, the Hamiltonian then reads

$$H = \begin{pmatrix} 0 & 0 & 0 & 0 & 0 & 0 \\ 0 & 0 & 0 & 0 & 0 & 0 \\ 0 & 0 & \Delta_{614} & 0 & \frac{\Omega_{614}}{2} & 0 \\ 0 & 0 & 0 & 0 & 0 & \frac{\Omega_{416}}{2} \\ 0 & 0 & \frac{\Omega_{614}}{2} & 0 & 0 & 0 \\ 0 & 0 & 0 & \frac{\Omega_{416}}{2} & 0 & \Delta_{416} \end{pmatrix} \tag{4.2}$$

Here, $\Omega_{614}$ and $\Omega_{416}$ are the Rabi frequencies of the pump (614 nm) and Stokes (416 nm) fields, respectively, and $\Delta_{614}$ and $\Delta_{416}$ denotes the detuning for each wavelength.

### Static case

For the first simulation, both fields were modeled as continuous and on resonance ($\Delta_{614,416} = 0$), making $\Omega_{416}$ and $\Omega_{614}$ constant. In the experiment, this corresponds to switching on both lasers at $t = 0$. With available laser powers of approximately 6.5 mW for both wavelengths, the Rabi frequency limits were set to $\Omega_{416} = 70\,\mathrm{MHz}$ and $\Omega_{614} = 80\,\mathrm{MHz}$. The Rabi frequencies where hereby approximated with reference to the Rabi frequencies used in Sec. 4.3.3. The 416 nm laser system in our laboratory is able to output more laser power then the 614 nm laser system, thus, configurations requiring less 614 nm power are preferred.
The initial state was chosen to be $5D_{5/2}$, ensuring that decay to $6S_{1/2}$ from $6P_{3/2}$ removes the ion from the preparation cycle. Additionally, decay from the $6P_{1/2}$ state was not allowed

in the simulation. Hence, the number of emitted 389 nm photons corresponds to the $6P_{1/2}$ population at the end of the cycle. This allows to optimize the emission of 389 nm photons by optimizing the final $6P_{1/2}$ state population. The master equation (2.27) was solved using the QuTiP package in Python [69], incorporating Lindblad terms for all relevant collapse operators and decay rates. The dynamics were simulated for different pump laser Rabi frequencies $\Omega_{614}$ and $\Omega_{416}$. The resulting heatmap showing the final $6P_{1/2}$ population as a function of both laser powers is shown in Fig. 4.2 a.). The optimal Rabi frequencies in the continuous case are $\Omega_{614} = 43$ MHz and $\Omega_{416} = 80$ MHz, corresponding to laser powers of $P_{614} = 1.87$ mW and $P_{416} = 6.46$ mW, respectively. The resulting population dynamics for these parameters are shown in Fig. 4.2 b.), with a state preparation probability exceeding 76.28 %.

### Semi-static case

In the second configuration, the 416 nm laser remained continuous while the 614 nm laser was pulsed. The 614 nm pulse was modeled as a Blackman window, which closely resembles a Gaussian profile but goes exactly to zero at the edges. With the AOM rise time of approximately 35 ns, the total pulse duration was set to 5 µs (full width from start to finish).
The simulation was repeated for different values of $\Omega_{614}$ and $\Omega_{416}$, with both lasers detuned by 5 MHz from their respective transitions. The resulting $6P_{1/2}$ populations are shown in Fig. 4.2 c.). The optimum was found at $\Omega_{614} = 80$ MHz and $\Omega_{416} = 70$ MHz, corresponding to $P_{614} = 6.46$ mW and $P_{416} = 6.69$ mW, respectively. However, efficiencies exceeding 78 % were already achieved with $\Omega_{614} = 43$ MHz ($P_{614} = 1.87$ mW). The population dynamics for the optimal Rabi frequencies are shown in Fig. 4.2 d.), where the state preparation probability reaches 78.26 %.
Varying the detuning between 0 MHz and 5 MHz had little effect on the final population, while larger detunings degraded performance. This indicates that moderate detuning in this configuration does not significantly improve the state preparation efficiency.

### STIRAP case

Because the $6P_{3/2}$ state is the main loss channel, a STIRAP sequence, in which the 416 nm (Stokes) pulse precedes the 614 nm (pump) pulse, should in theory suppress intermediate state population and thus losses. To test this, both lasers were pulsed, and their shapes were optimized using the Krotov algorithm [70] to maximize $6P_{1/2}$ population.
The optimization was constrained so that the peak Rabi frequencies did not exceed $\Omega_{614} = 80$ MHz and $\Omega_{416} = 70$ MHz, reflecting realistic experimental limits. After 2000 optimization iterations, a final state fidelity of 76.1 % was achieved, which is comparable to the static case. This result suggests that, under the given constraints, STIRAP does not significantly outperform the simpler static approach in terms of efficiency.

The simulations show that all three cases achieve a state preparation probability exceeding 75 %. However, the static and semi-static cases require less technical overhead to implement in practice compared to a STIRAP scheme, which is why the latter is not pursued in the experiment. Among the tested approaches, the semi-static case with a pulse duration of 5 µs for the 614 nm laser, and laser powers of $P_{416} = 6.69$ mW and $P_{614} = 1.87$ mW, yields the highest efficiency with a state preparation probability of 78 %, making it the most effective method for the pumping process.

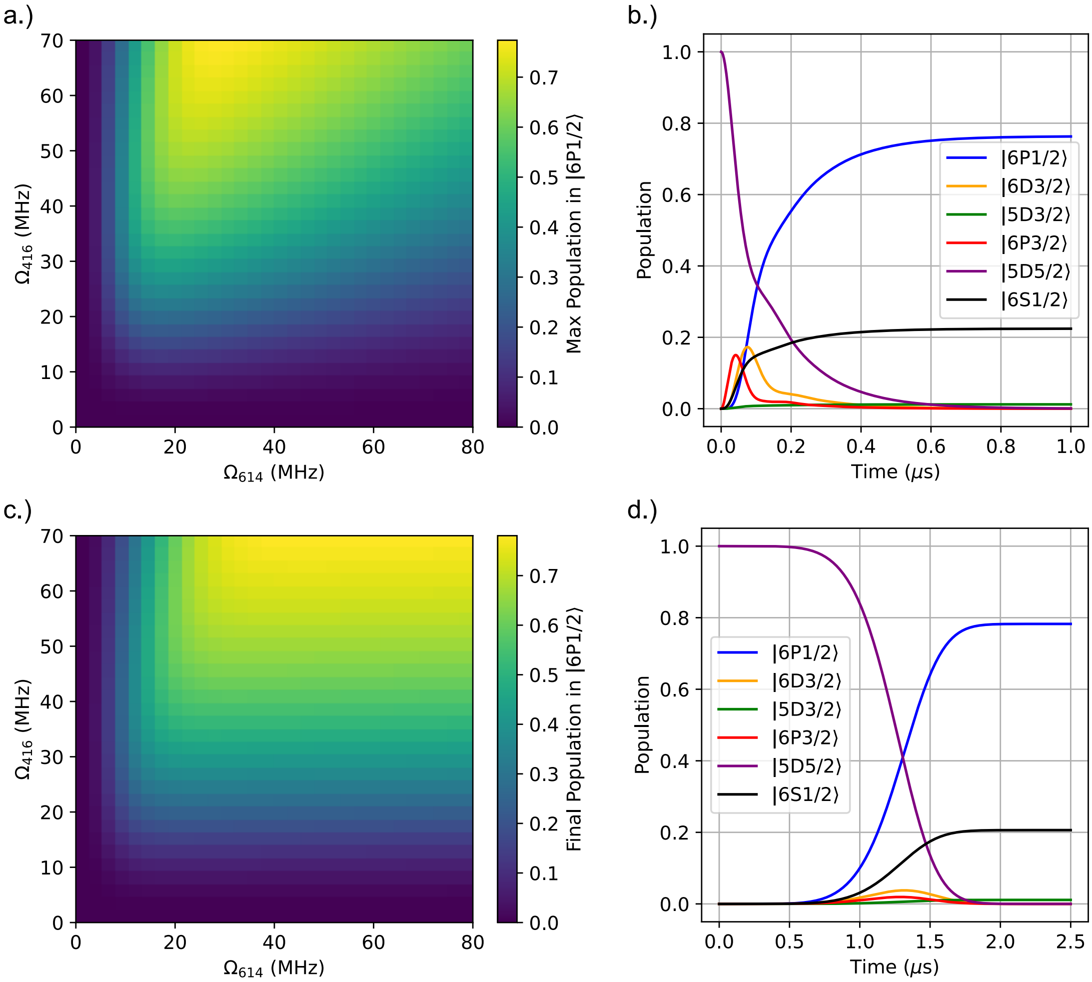

**Figure 4.2:** The simulation results for different state preparation schemes. a.): A heatmap of the final $6P_{1/2}$ state population for the static case with both lasers continuously on, as a function of $\Omega_{614}$ and $\Omega_{416}$. b.): The time evolution of the relevant state populations for the static case at the optimal Rabi frequencies $\Omega_{614} = 43\,\mathrm{MHz}$ and $\Omega_{416} = 80\,\mathrm{MHz}$. The final state preparation probability exceeds 76 %. c.): A heatmap of the final $6P_{1/2}$ state population for the semi-static case, with the 614 nm laser pulsed and the 416 nm laser continuous. d.): The time evolution of the relevant state populations for the semi-static case at the optimal Rabi frequencies $\Omega_{614} = 80\,\mathrm{MHz}$ and $\Omega_{416} = 70\,\mathrm{MHz}$. The final state preparation probability exceeds 78 %. The simulations include spontaneous decay via Lindblad terms, with parameters matched to realistic experimental constraints.

## 4.3 Experimental setup

Three lasers are required to pump the ion from the ground state to the $6D_{3/2}$ state for state preparation. The 416 nm laser enters the vacuum chamber together with the second PI laser from the right-hand side of the laser table, as described in Sec. 3.3.2. The 1.7 µm beam enters the vacuum chamber via a viewport located at the bottom of the vacuum vessel. A lens with focal length of f=150 mm mounted outside the vacuum chamber was used to focus the infrared light on the ion. At resonance, the 1.7 µm light induced quantum jumps that could be identified by intervals of interrupted fluorescence emission corresponding to the conditions in which the ion is in the $5D_{5/2}$ state.

A sketch of the vacuum chamber with the complete detection setup is shown in Fig. 4.3. On the right hand side of the vacuum chamber, the new part of the detection setup was placed. The light emitted by the ion was collected by a lens (L2) with a focal length of $f = 25\,\mathrm{mm}$ and an numerical aperture of 0.4. The first two lenses outside of the vacuum chamber (L3 with $f = 150\,\mathrm{mm}$ and L4 with $f = 25\,\mathrm{mm}$) build a telescope to resize and collimate the emitted light cone. In between L3 and L4, an iris is placed in order to remove scattering light caused by the Doppler cooling beams hitting the trap blades. The collimated light then struck the first of two dichroic mirrors (DM1), a long-pass filter with a cutoff wavelength of 425 nm. This allowed the separation of 493 nm and 650 nm light from the 389 nm photons. The 389 nm photons will be directed via another mirror (M2) through a lens (L5) and focused onto the detection area of an avalanche photodiode (APD 389). The 493 nm and 650 nm light were separated via a second long-pass dichroic mirror (DM2), which had a cut off wavelength of 550 nm, enabling the spatial separation of 493 nm and 650 nm photons. Each beam was then directed to its respective mirror (M3 and M4), passed through a lens (L6 and L7), and detected by a separate APD (APD 493 and APD 650).

### 4.3.1 Alignment of the 493 nm APDs

On the left-hand side of the vacuum vessel is the old detection setup. Using a rotatable wheel on a switch box, it is possible to toggle the detection method between an EMCCD camera and a fiber-coupled APD. The fiber connected to the APD is aligned through a fiber collimator, which is mounted on a piezo stage. This setup allows precise adjustments of the collimator's position via computer control. When the fiber APD is misaligned, the first step is to trap a single ion, which is detectable with the EMCCD camera positioned on the left side of the setup. On the right-hand side, a regular mirror is installed instead of L4, allowing the ion's emitted light to reflect back onto itself. By adjusting the screws on the mirror mount, the mirror image can be aligned directly on top of the ion. Once the mirror image and ion are aligned, the next step is to turn the switch box's wheel on the left-hand side of the chamber, guiding the fluorescence of the ion to the fiber APD. Then, a fiber carrying 493 nm light is connected to the fiber collimator of the fiber APD. The laser beam travels through the vacuum chamber and reflects back off the mirror on the right-hand side. At this stage, the incoming and outgoing beams must be overlapped as closely as possible to optimize the fiber collimator's position. After overlapping the two beams, the back-reflecting mirror on the right side is blocked again, and the fiber APD is reconnected to the now semi-aligned collimator. Once the APD is switched on, the collimator alignment can be scanned. At a certain point, a spike in the photon counts will appear, corresponding to photons emitted by the single ion. This signal can be further optimized by fine-tuning the collimator's position. The alignment method introduced below for the new detection setup relies on first completing the alignment of the old fiber APD setup.

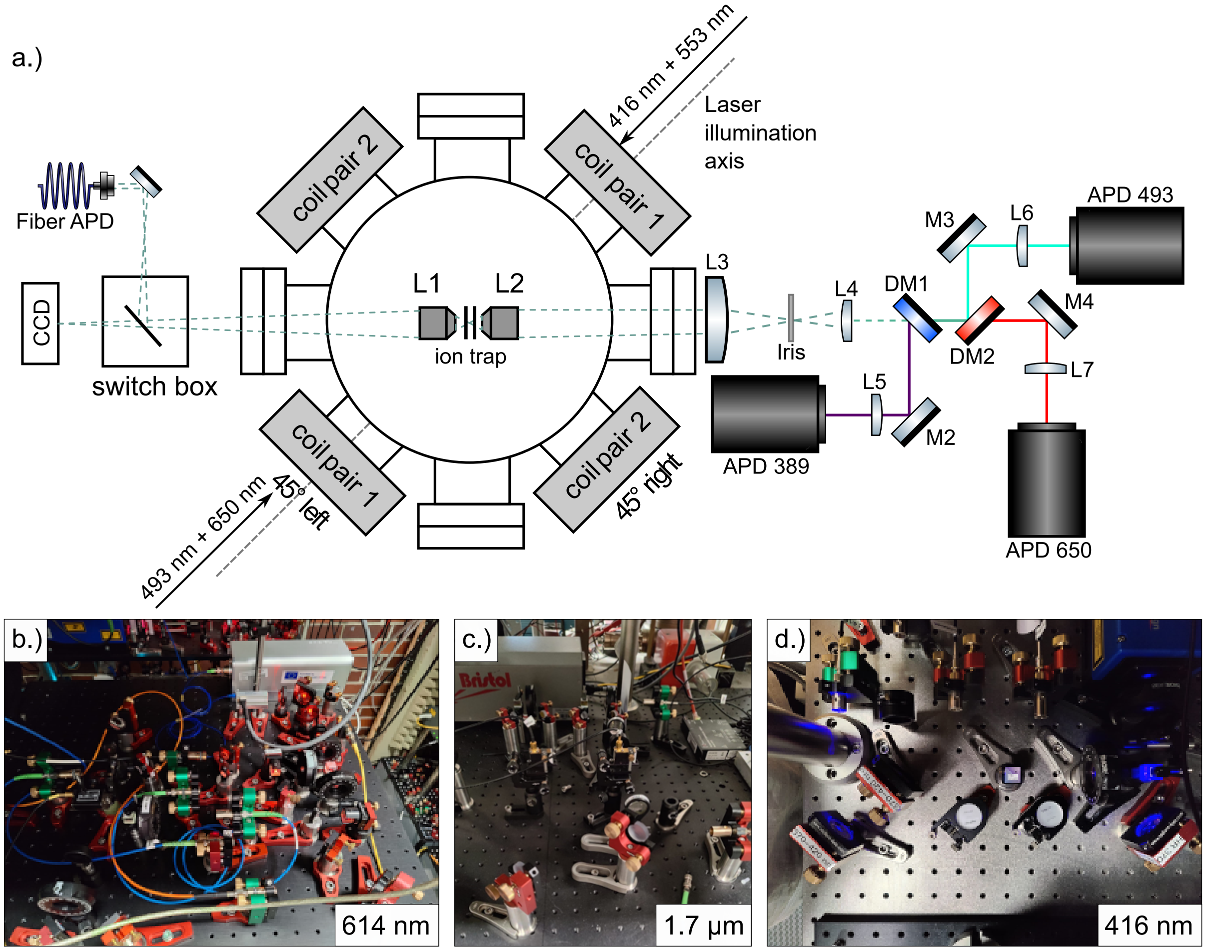

**Figure 4.3:** a.): The vacuum vessel housing the linear Paul trap and the two detection setups positioned on either side of the vacuum chamber. The two Halo-lenses (L1 and L2) with a focal length of 25 mm and a numerical aperture of 0.4 collimate the ions fluorescence. The Helmholtz coils (coil pair 1 and coil pair 2) are used to adjust the magnetic field in the horizontal plane. The figure is inspired by Ref. 33. On the right-hand side, the APD system realized and tested during this work is displayed. A combination of two lenses (L3 and L4) with focal lengths of $f$ =150 mm and $f$=75 mm form a telescope to shrink the beam diameter. Two dichroic mirrors (DM1 and DM2) are used to separate the photons emitted by the ion at different wavelengths. The corresponding beam paths are colored according to the photon wavelength, which is specified in the label of the APDs at the end of each beam path. Three additional mirrors (M2, M3, and M4) guide each separated beam through lenses (L5, L6, and L7) onto the detection area of the APDs. On the left-hand side of the vacuum chamber, the pre-existing detection setup is shown. This setup includes a switch box that allows the user to alternate between a CCD camera and a fiber-coupled APD (fiber APD) for ion detection. b.): A photo of the optics of the 614 nm laser system needed for pumping the ion from the $5D_{5/2}$ state into the $6D_{3/2}$ state. c.): A photo of the optics of the 1.7 µm laser system used to populate the $5D_{5/3}$ state starting from the $6S_{1/2}$ state. d.): A photo of the optics of the 416 nm laser system used to populate the $6D_{3/2}$ state.

To begin the alignment of the new detection setup, a fiber carrying 493 nm light is attached to the already aligned fiber collimator of the APD. On the right-hand side of the chamber, the light is deflected into the APD detection system. The first dichroic mirror (DM1), transmits the 493 nm light, while the second dichroic mirror (DM2) deflects the beam. The 493 nm beam then hits a mirror (M3) that directs the light through a lens (L6) onto the detection area of the first APD. The lens is mounted on a micrometer translation stage, allowing precise focus adjustment. Once the optimal focus is achieved, neutral-density (ND) filters are added to reduce the beam power until it is barely visible to the naked eye. The APD is then switched on, and the photon signal of the laser beam is detected. If the signal becomes saturated, the beam path is blocked, and additional ND filters are applied. When a non-saturated signal is detected, the alignment of the final mirror and the position of the lens before the APD are adjusted for optimization. The APDs themselves are additionally mounted on a translation stage, allowing for further fine-tuned adjustments in their position. At this stage, the ND filters can be removed from the system and a single bandpass filter, with a central wavelength of 490 nm and a FWHM = 10 nm is put in front of the APD. When a single ion is trapped and if the alignment is correct, a change in the photon countrate detected by the APD is observed when the 650 nm repumper is aligned with the ion vs when it is chopped. Additionally, a difference in the signal is noticeable when the trap is loaded compared to when it is empty. This provides a way to further optimize the alignment of the final mirror (M3) and the focus of the lens (L6) before the APD (APD 493).

### 4.3.2 Alignment of the 650 nm APD

We attempted to repeat the alignment method described in Sec. 4.3.1 for the 650 nm free-space APD. We replaced the 493 nm light exiting the collimator of the fiber-coupled APD with 650 nm laser light. The 650 nm light was directed through the vacuum chamber and exited into the newly built APD system. The light then passed through both dichroic mirrors (DM1 and DM2), was deflected by an additional mirror (M4), and focused by a lens (L7) into the APD (APD 650).

However, the number of 650 nm photons emitted is about one quarter of the number of photons emitted at 493 nm. This implies that the signal-to-noise ratio of the detection system at 650 nm may be too low to allow for effective alignment optimization using the ion. Consequently, a custom filter holder for the APDs was designed. A CAD drawing of the holder is shown in Fig. 4.4 a.). This holder allows a filter to be mounted directly onto the APD, minimizing stray light. Moreover, the holder can be mounted without disturbing the optical alignment, making it possible to exchange filters in front of the APDs without altering the detection setup.

A second issue with this alignment method is that the focal points for 650 nm and 493 nm light differ significantly. This indicates that our detection system is not achromatic, which is particularly problematic given the small effective detection area of the APDs, which is only 50 $\mu m^2$. Therefore, the same alignment strategy described before could not be directly applied to the 650 nm APD.

We were able to detect 493 nm fluorescence from a single ion on a second EMCCD camera (Andor-Luca) when it was positioned at the location of the 650 nm APD, both dichroic mirrors were removed and a bandpass filter with a central wavelength of 490 nm and a FWHM of 10 nm was introduced in front of the camera lens. The bigger detection area of the camera of 8 $mm^2$ allowed us to detect 650 nm light emitted from a single ion once the final lens was moved farther from the camera and the 493 nm filter was exchanged with a bandpass filter with a central wavelength of 650 nm and a FWHM of 10 nm (650 nm filter). This additional detection possibility allowed us to align the 650 nm APD via the following procedure:

- The camera was exchanged for the 650 nm APD, and a flip mirror was inserted directly in front of the APD so that fluorescence could be redirected to the camera when required (see Fig. 4.4 b.)).
- The APD was aligned to the ion using the 493 nm emission, following the procedure described in Sec. 4.3.1. To ensure spectral selectivity, a 493 nm bandpass filter was placed in front the APD.
- The flip mirror was used to redirect the light emitted by the ion onto the detection area of the EMCCD camera.
- The distance between the flip mirror and the camera was adjusted by moving the camera, until the ion appeared focused on the camera image. This ensures that the optical path length to the camera and the APD matches.
- The filter in front of the camera was replaced with a 650 nm bandpass filter, and the final lens position was fine-tuned to bring the 650 nm fluorescence into focus.
- The final mirror before the lens was adjusted so that the 650 nm image appeared at the same position on the camera sensor as the previously aligned 493 nm image.
- The filter in front of the APD was exchanged for the 650 nm bandpass filter and the flip mirror was removed. This allowed us to observe a signal via the APD. Blocking the 493 nm laser extinguished the signal, confirming that the detected counts originated from single 650 nm photons.
- The APD signal was optimized, and the flip mirror was permanently extracted from the beam path.

### 4.3.3 Test of the alignment

As already highlighted in the previous chapter, the small detection area of the free-space APDs of only 50 µm$^2$ makes it challenging to align the detectors onto a single ion. The alignment method described in Sec. 4.3.1 and Sec. 4.3.2 was tested by performing correlation measurements between the old fiber APD and the newly installed 493 nm and 650 nm APDs. In Fig. 4.5, a sketch for this measurement is depicted as well as the three outcomes of the two-photon correlation function $g^{(2)}$.

In case a.), the correlation function is at its maximum at zero delay time ($\tau = 0$) and gets smaller for larger time delays ($\tau > 0$). This means that the probability of a second photon event after a small time period is higher than for longer time delays, i. e. the photons emitted by the light source arrive on the APDs preferably in packets of multiple photons. This effect is called bunching and can occur for example, if you use a thermal light source.

In the second case b.), the correlation function is constant over all different time delays, which implies that the incoming photons are not correlated with each other. This behaviour occurs for example if you use a laser as a light source.

The behaviour of the second order correlation function for a single ion, as observable in our experiment, is called antibunching. Antibunching of the resonant fluorescence can be interpreted as follows. Here, only a single photon gets emitted by the light source at a time. Thus the correlation function has a minimum at a time delay of $\tau = 0$, as depicted by c.). By detecting an antibunching behaviour, we can verify the alignment of the new 493 nm and 650 nm APD on

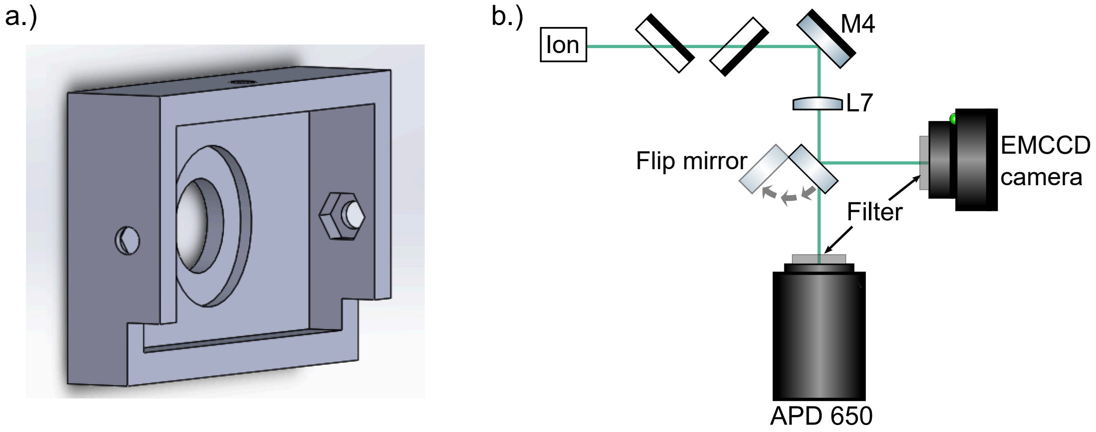

**Figure 4.4:** a.): A CAD drawing of the newly designed filter box for the free-space APDs. The filter box allows for rapid filter exchange without disturbing the rest of the detection setup. b.): The adjusted detection setup for aligning the 650 nm APD. The procedure begins by aligning the APD using 493 nm fluorescence from the ion. A flip mirror is then inserted into the beam path to direct the light onto an EMCCD camera mounted on a translation stage, which is adjusted until the ion image is in focus. The filter in front of the camera is subsequently replaced to allow detection of 650 nm photons. By adjusting the position of lens L7, the 650 nm photons can be focused onto the camera, and fine-tuning mirror M4 ensures that the 650 nm image aligns with the previously observed 493 nm image. Finally, the flip mirror is removed, the filter in front of the APD is exchanged, and a signal from 650 nm photons can be observed on the APD.

the ion. The measurement of the $g^{(2)}$ function is proportional to the excited state population (Eq. 2.46) that is evolving over the time $\tau$ under the condition that at time zero ($\tau = 0$) the atom is projected into the ground state state. It is not possible for the ion to emit a photon if it is in the ground state, thus it is not possible for a two photon event to occur at zero delay time. The ion first needs to be re-excited into the first excited state by a driving light-field. From there, it can again fall back into the ground state and emit a second photon. This behaviour corresponds to a dip at $\tau = 0$ in the second order correlation function and is a common effect for non-classical light sources. For an antibunching correlation function in an ideal case, $g^{(2)}(0) = 0$ holds.
For the first measurement of the second order correlation function, the fiber APD and the APD 493 nm were used in order to test the alignment method for the APD 493 nm described in Sec. 4.3.1. Both detection setups at the two sides of the ion trap where darkened by black cardboard and fabric in order to minimize background and thus optimize the signal to noise ratio. Additionally, all the computer screens in our lab were darkened during the measurement. Both APDs were connected to a time tagger which functions as a time correlator between two channels. The signals of the new 493 nm APD was used as the reference to correlate the incoming counts of the old fiber APD. The resolution of the correlator was set to 1 ns. This parameter defines the bin size in which the correlator sorts the time differences between the detection of two photons. For example, if two detection events occur with delays of 1.1 ns and 1.7 ns, they are assigned to the 1 ns and 2 ns bins, respectively. If instead bigger bin size, e.g., 1 µs, were chosen, both events would fall into the same bin. In this way, the chosen bin size determines the temporal resolution with which the correlation function is recorded. For this measurement photon arrival time differences from −250 ns up to 300 ns were detected over a time span of about four hours.

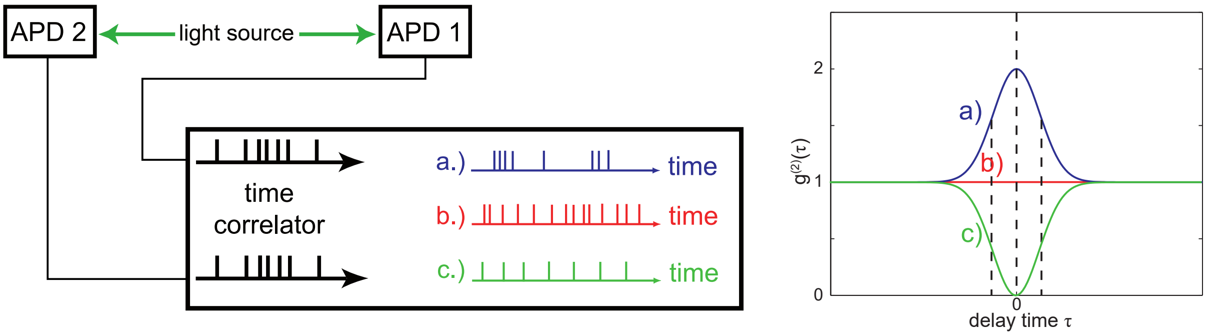

**Figure 4.5:** The experimental setup for a Hanbury-Brown and Twiss (HBT) measurement [71]. The setup consists of two detectors (APD 1 and APD 2), which are used to detect signals from a light source. The detected signals are subsequently correlated to analyze photon arrival characteristics. Depending on the nature of the light source, three possible outcomes arise: a.) Bunching behavior is observed, characterized by a positive peak in the second-order correlation function $g^{(2)}(\tau)$. b.) A random photon arrival pattern results in a flat correlation function, indicating no particular photon correlation. c.) Antibunching behavior, typically associated with quantum single-photon emitters such as single ions, leads to a minimum at $\tau = 0$ in the correlation function, indicating that two photons are unlikely to arrive simultaneously.

With the collected data points, the histogram depicted in Fig. 4.6 a.) was created. The standard deviation calculated as the square root of the number of counts for each bin was used as a statistical error. The local minimum indicates the antibunching behaviour typical for ions. Datapoints with a time delay bigger than 25 ns were used to create an exponential fit with formula $y = a \cdot \exp(-\tau \cdot b) + c$. The threshold of 25 ns was chosen because at this delay the $g^{(2)}$ function exhibits a local maximum. For larger delays, the function follows an exponential decay. The offset $c$ of the resulting function was used for normalization and its standard deviation $\sigma_c$ was used to estimate the confidence interval of the simulated function ($\sigma_c/c = 0.14$). The resulting errors of the fit are used to define a confidence interval for the following $\mathrm{g}^{(2)}$ simulation.

The correlation function was simulated by solving the master equation for a three level system using Eq.(2.46) and the QuTip python package [69]. Based on the measurement, the saturation parameters where chosen to be $s_g = 0.8$ and $s_r = 0.75$ for the 493 nm and the 650 nm laser, respectively and laser detunings of $\Delta_g = -6\,\mathrm{MHz}$ and $\Delta_r = -5\,\mathrm{MHz}$ were chosen for the simulation.

Correlation measurements between the 493 nm and 650 nm free-space APDs were performed, to test the alignment method described in Sec. 4.3.2. The newly designed filter box (Fig. 4.4 a.)) was used to place a 493 nm and a 650 nm filter in front of the respective detectors. In order to further optimize the signal-to-noise ratio, the detection setup was additionally shielded with black cardboard and fabric. The computer screens in the laboratory were also darkened, as in the previous measurement. Both APDs were connected to the time tagger to record time differences between the detected 493 nm and 650 nm photons. The resolution of the correlator was again set to 1 ns. This time, correlations were measured for time differences from −250 ns to 250 ns. Furthermore, since the ion remained stable in the trap for a longer duration, the acquisition time could be extended to about six hours.

The collected data are shown in Fig. 4.6 b.). Owing to the implemented filter box, the measured signal exhibited reduced fluctuations compared to the correlation measurement between the fiber APD and the 493 nm free-space APD. As a result, the baseline was clearly defined as data with $|\tau| > 200\,\mathrm{ns}$. This choice was made because, at time differences larger than 200 ns, the system

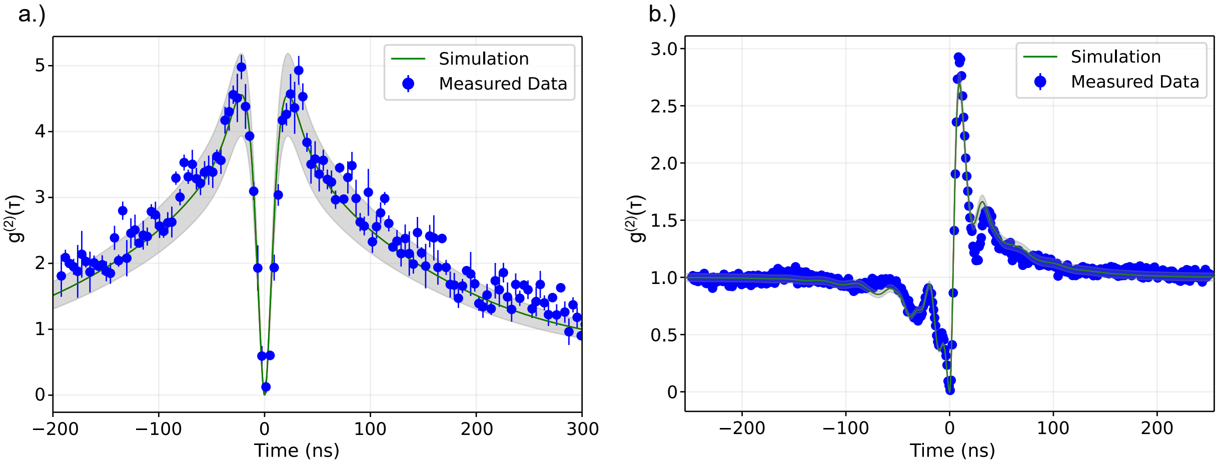

**Figure 4.6:** The measurements of the second-order correlation function $g^{(2)}(\tau)$ of a single Ba ion, which exhibits antibunching behavior. Both functions depicted were determined by solving the master equation for a laser driven three level system. a.): The correlation function measured with the 493 nm fiber APD and the 493 nm free space APD. It was simulated with $s_g = 0.4$, $s_r = 0.26$, $\Delta_g = -6\,\text{MHz}$ and $\Delta_r = -5\,\text{MHz}$. The gray area indicates the confidence interval of the simulation determined by the uncertainty of the data. This uncertainty changes the limiting value for $\tau \to \infty$ that is used to normalize the correlation function. This limit was estimated with an exponential fit to the data points with $\tau > 25\,\text{ns}$. b.): The correlation function measured with the 493 nm and 650 nm free space APD. It was simulated with $s_g = 2.5$, $s_r = 0.09$, $\Delta_g = -10\,\text{MHz}$ and $\Delta_r = -35\,\text{MHz}$

has certainly reached the steady-state limit. Consequently, the error bars of the datapoints could be defined as the standard deviation of the measured baseline signal. Additionally, the baseline signal was used for normalisation.
The system was simulated by solving the master equation using the QuTip Python package [69]. Due to the different transitions that the photons of different color originated, the correlation measurement of these photons is asymmetric. We simulated the excited state population over time starting from different initial conditions, to represent this physical mode. For values $\tau > 0$, the $6S_{1/2}$ state was selected as initial state. In contrast, for $\tau < 0$, the metastable $5D_{3/2}$ state was chosen to be the initial state. The saturation parameters for the simulation were $s_g = 2.5$ and $s_r = 0.09$ for the 493 nm and 650 nm lasers, respectively and the detunings were set to $\Delta_g = -10\,\text{MHz}$ and $\Delta_r = -35\,\text{MHz}$ to agree with the measured data.

The agreement between the measured data and the simulations of the system dynamics demonstrates that both alignment methods for the free-space APDs are effective. In both cases, the measurements show clear antibunching behavior, as expected. The symmetry around the time axis observed in the correlation between the two 493 nm APDs, as well as the asymmetric shape of the second $g^{(2)}$ function showing the correlation between the 493 nm and 650 nm APDs, confirm that the detectors were aligned properly.

## 4.4 Outlook

The experiments and simulations developed over the course of this thesis establish a foundation for a range of future quantum optics and quantum information experiments. The immediate next step in verifying the functionality of the proposed state preparation scheme will be performing spectroscopy on the $6P_{3/2} \rightarrow 6D_{3/2}$ transition in $^{138}Ba^{+}$. This can be achieved by detecting the 389 nm photon emitted via spontaneous decay from the $6D_{3/2} \rightarrow 6P_{1/2}$ state. Tracking this photon allows for the fine-tuning of pumping parameters, thereby reducing the state preparation time and minimizing population loss during measurements. The simulation presented in this thesis provides an informed starting point for optimizing laser parameters for these upcoming experiments. Moreover, the APD alignment techniques developed here should be directly applicable to experiments within the Panopticon apparatus [45]. In the Panopticon setup, the focus shifts toward controlling the spontaneous emission of a single $^{138}Ba^{+}$ ion using a hemispherical mirror as a reflective boundary condition for the optical radiation. The ion will be positioned at the mirror's center of curvature, as illustrated in Fig. 4.7 a.). When an ion emits a photon, the mirror reflects it back onto the ion, resulting in either constructive or destructive interference depending on the mirror's radius. With an numerical aperture (NA) of 1, spontaneous emission can be entirely suppressed due to destructive interference of the standing wave emitted by the ion with itself. This condition holds when the radius $R$ of the mirror satisfies

$$R = n\frac{\lambda}{2}, \tag{4.3}$$

where $n$ is an integer and $\lambda$ represents the photon's wavelength. Alternatively, placing the ion at an anti-node of the vacuum mode results in enhanced spontaneous emission, which occurs when

$$R = n\frac{\lambda}{2} + \frac{\lambda}{4}. \tag{4.4}$$

A graph illustrating the modification of the spontaneous emission rate as a function of the mirror's numerical aperture is shown in Fig. 4.7 b.).

The Panopticon apparatus enables the extension of excited state lifetimes based on the radius of the hemispherical mirror. A mirror mount that incorporates heating wires, allows us to adjust the mirror's radius through thermal expansion. By running current through the heating wires, the system heats up, causing the mirror to expand. This thermal expansion modifies the distance between the mirror's surface and the ion at its center. An expected change in the mirror's radius is on the order of micrometers per degree Celsius [72]. Figure 4.8 a.) illustrates the mirror mount equipped with the heating wire. We focus particularly on the decay of the $6P_{1/2}$ state in $^{138}Ba^{+}$, which decays into the $6S_{1/2}$ state by emitting a 493 nm photon or into the $5D_{3/2}$ state by emitting a 650 nm photon. Since the suppression of spontaneous emission is dependent not only on the mirrors radius but also on the wavelength, we can modify the natural branching ratio of the $6P_{1/2}$ state in $^{138}Ba^{+}$ by adjusting the mirror's radius. For a precise measurement of the branching ratio in dependence of the mirror's radius, the proposed heralding state preparation scheme can be employed. The emitted 389 nm photon must be correlated with the respective secondary 650 nm or 493 nm photon, resulting in two exponential decay curves from which the branching ratio can be extracted. Figure 4.8 b.) shows the decay rate of the $6P_{1/2}$ state into both the $6S_{1/2}$ and $5D_{3/2}$ states as a function of the mirror's radius.

Monte Carlo simulations were used to model individual quantum trajectories of a continuous drive and count the occurrences of quantum jumps corresponding to the collapse operators during each quantum trajectory. This approach enabled the determination of the time delay, $\tau$, between the

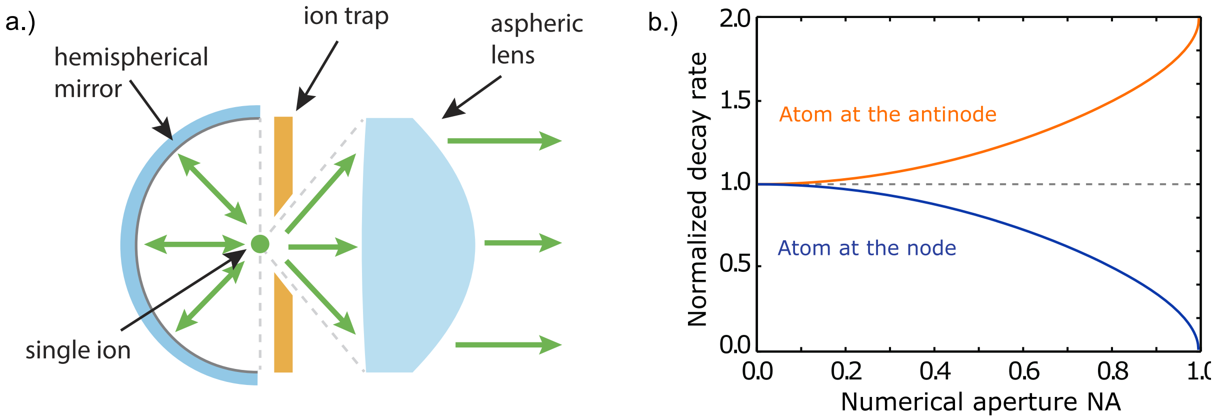

**Figure 4.7:** Both figures where taken from [45]. a.): A sketch of the main components in the Panopticon apparatus. A planar ring trap is used to confine a single $^{138}$Ba ion. An aspheric lens with a high numerical aperture (0.7) is positioned on one side for efficient photon detection, while a hemispherical mirror on the opposite side introduces a boundary condition to modulate spontaneous emission. b.): A plot of the normalized decay rate as a function of the mirror's numerical aperture (NA). Complete suppression of spontaneous emission is possible at an NA of 1 when the ion is positioned at a vacuum mode node, while positioning the ion at an anti-node enhances emission.

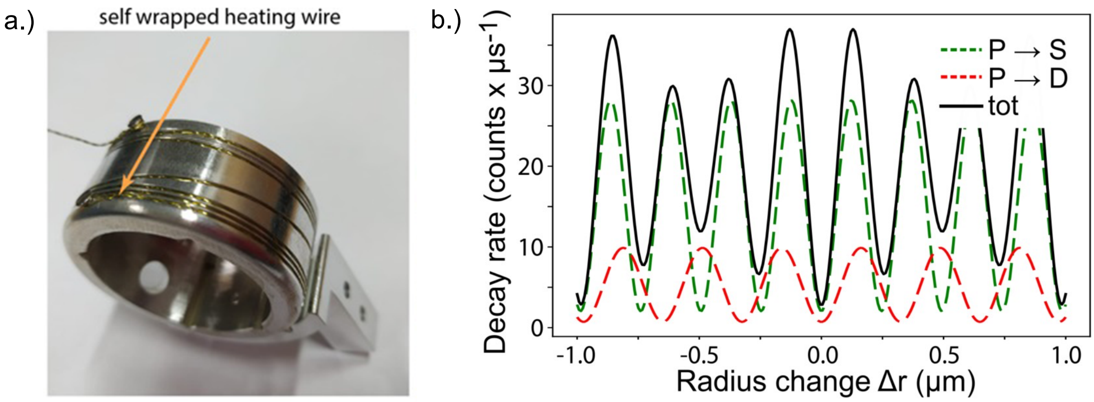

**Figure 4.8:** a.): The mount for the hemispherical mirror. The heating wires enable adjustment of the mirror's radius through thermal expansion. b.): The varying decay rates of the $6P_{1/2}$ state in $Ba^+$ as a function of the mirror's radius. The green line represents the decay rate into the $6S_{1/2}$ ground state, while the red line indicates the decay rate into the $5D_{3/2}$ state. The black line denotes the total decay rate.

detection of a 389 nm photon and the subsequent detection of either a 650 nm or 493 nm photon. The resulting decay rates from the $6P_{3/2}$ state to the $5D_{3/2}$ state, along with a conceptual sketch of the measurement setup required to produce this data, are depicted in Fig. 4.9. The simulation here were produced using the QuantumOptics.jl package [73].

For further testing, the next step is to measure these two exponential decays to determine the branching ratio of the $6P_{1/2}$ state in the linear trap. The detection setup has been constructed to facilitate direct placement next to the Panopticon apparatus. Initially, a test measurement will be conducted to simplify the installation of the APD system. Subsequently, a measurement of the branching ratio as a function of the mirror's radius can be performed. Furthermore, the time constant of the exponential decay can be evaluated to measure the influence of the hemispherical mirror on the $6P_{1/2}$ lifetime.

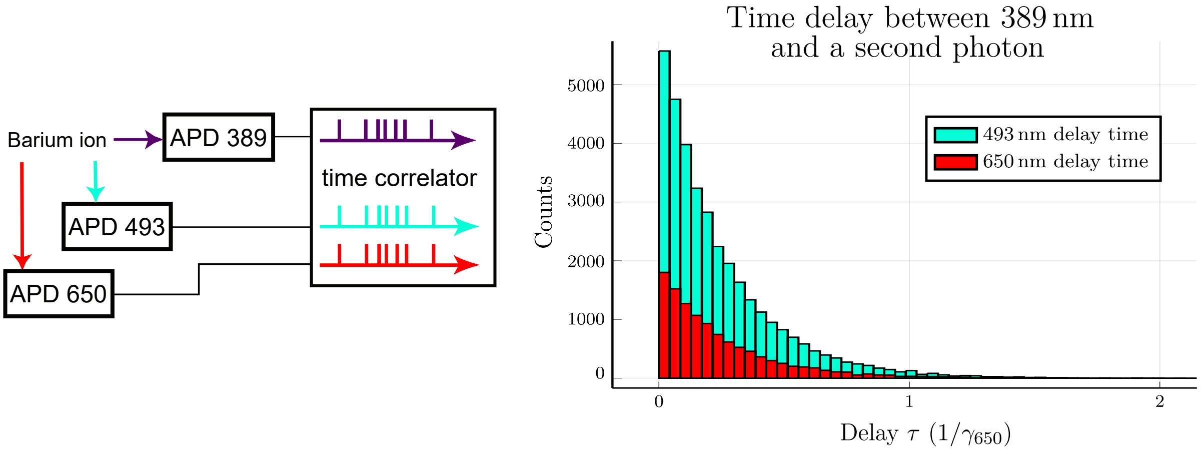

**Figure 4.9:** The proposed measurement scheme to observe the variation of the lifetime and the branching ratios of the $6P_{1/2}$ state decay into the $6S_{1/2}$ and $5D_{3/2}$ states. A detected signal at the 389 nm APD is correlated with signals from the 493 nm and 650 nm APDs, respectively. The time delay between detections will reflect an exponential decay into the two branching channels. The graph on the right-hand side illustrates the results of a Monte Carlo simulation with 100001 iterations, showing the expected decay behavior.

# 5 Conclusion

This thesis has presented the implementation of a resonantly enhanced multi-photon ionization (REMPI) scheme for the isotope selective trapping of single $Ba^+$ ions and proposed a novel heralded state preparation scheme for quantum optics experiments. Key developments included the construction of an ionization test chamber, the installation and characterization of a new 416 nm laser, and the augmentation of three optical assemblies, including a detection setup for measuring the branching ratios of the $6P_{1/2}$ state.

After introducing the theoretical framework required for the experiments and simulations carried out in this thesis, the second chapter focuses on the construction and optimization of an ionization test chamber. This chamber was designed to evaluate the newly developed oven mount and to demonstrate the isotope selectivity of the 553 nm transition ($6s^2\ ^1S_0 \rightarrow 6s6p\ ^1P_1$) in neutral Ba. As results of this experiment, the thesis presents the final design of the oven and ablation target holder currently assembled in the Panopticon apparatus and the fluorescence spectroscopy of the $6s^2\ ^1S_0 \rightarrow 6s6p\ ^1P_1$ transition in neutral Ba. Scanning the laser frequency revealed a spectrum in which four peaks were observed. The two primary peaks corresponded to the isotopes $^{138}Ba$ and $^{136}Ba$, with abundances of 71.7 % and 7.9 %, respectively, while additional peaks were attributed to $^{137}Ba$ and $^{135}Ba$ isotopes.
Following this, a thorough description of the trapping process within the linear Paul trap was provided, which included the installation and fine-tuning of the new 416 nm laser and the alignment of the second PI laser at 553 nm. By superimposing the PI lasers with the Doppler cooling beams, we ensured that Doppler cooling commenced at the same location as the ionization process. A simulation of the ionization probability, as a function of the 553 nm laser frequency, indicated that tuning the laser to lower frequencies improved the selectivity for trapping $^{138}Ba^+$ ions. It was shown, that the new REMPI scheme exploiting the 553 nm transition ($6s^2\ ^1S_0 \rightarrow 6s6p\ ^1P_1$) exceeds the isotope selectivity of the scheme using the 413 nm transition ($6s^2\ ^1S_0 \rightarrow 5d6p\ ^3D_1$) the moment, an angle between the ionization lasers and the neutral Ba beam is introduced. Experimentally, we determined that a laser frequency of 541 433 150 MHz and a power of approximately 10 µW for the 553 nm beam yielded reliable trapping of single $^{138}Ba^+$ ions.

The third chapter of this thesis focused on a heralded state preparation scheme for populating the $6P_{1/2}$ state in a $Ba^+$ ion. Unlike traditional methods which populate the state using a short laser pulse, our approach leverages the spontaneous decay from the $6D_{3/2}$ state into the $6P_{1/2}$ state. During this decay, a 389 nm photon is emitted, providing a detectable signal that heralds the ion's state preparation. Achieving this photon detection required pumping the ion into the $6D_{3/2}$ state using 1.7 µm, 614 nm, and 416 nm lasers. Additionally, the optics for the 1.7 µm and 614 nm lasers were refined to allow frequency scanning, switching and ensuring that the ion was exposed to all required wavelengths. Simulations of static, semi-static, and STIRAP pumping schemes demonstrated that, under realistic laboratory conditions (laser powers of about 6.5 mW), the target state can be prepared with efficiencies of 76.28 % (static case), 78.26 % (semi-static case), and 76.1 % (STIRAP case).
A detection setup was established to capture the 389 nm photon, projecting the ion into the target

state upon detection. The APD-based detection system also included channels to monitor the secondary 493 nm or 650 nm photons, which may be emitted once the ion occupies the $6P_{1/2}$ state. This setup was validated through two measurements of the second order correlation function of an ion's resonant fluorescence.

Finally, an outlook for future quantum optics experiments was presented that build upon the experimental methods and simulations developed throughout this thesis. The discussion focused on the Panopticon setup, which allows control over the spontaneous emission of single $^{138}\mathrm{Ba}^{+}$ ions by introducing a boundary condition in the form of a hemispherical mirror. When a trapped ion emits a photon, the mirror reflects it back onto the ion, resulting in constructive or destructive interference depending on the emitted photon's wavelength and the mirror's radius. The ionization and state preparation schemes proposed in this thesis can be used to trap and prepare the ions in the excited $6P_{1/2}$ state. This state spontaneously decays either to the $6S_{1/2}$ state by emitting a 493 nm photon or to the $5D_{3/2}$ state by emitting a 650 nm photon. By changing the mirror's radius, the natural branching ratio between these two decay channels can be adjusted and controlled.

# Bibliography

[1] R. Blatt and C. F. Roos, “Quantum simulations with trapped ions”, Nature Physics **8**, 277–284 (2012).

[2] D. Leibfried, R. Blatt, C. Monroe, et al., “Quantum dynamics of single trapped ions”, Reviews of Modern Physics **75**, 281–324 (2003).

[3] H. Haffner, C. Roos, and R. Blatt, “Quantum computing with trapped ions”, Physics Reports **469**, 155–203 (2008).

[4] W. Paul, “Electromagnetic traps for charged and neutral particles”, Reviews of Modern Physics **62**, 531–540 (1990).

[5] W. Demtröder, *Laser Spectroscopy* (Springer Berlin Heidelberg, Berlin, Heidelberg, 1996).

[6] F. Schmidt-Kaler, C. Roos, H. C. Nägerl, et al., “Ground state cooling, quantum state engineering and study of decoherence of ions in Paul traps”, Journal of Modern Optics **47**, 2573–2582 (2000).

[7] E. Nir, M. Müller, L. Grace, et al., “Rempi spectroscopy of cytosine”, Chemical Physics Letters **355**, 59–64 (2002).

[8] E. Nir, L. Grace, B. Brauer, et al., “Rempi spectroscopy of jet-cooled guanine”, Journal of the American Chemical Society **121**, 4896–4897 (1999).

[9] M. Blumenstock, R. Zimmermann, K.-W. Schramm, et al., “Identification of surrogate compounds for the emission of PCDD/F (I-TEQ value) and evaluation of their on-line real-time detectability in flue gases of waste incineration plants by REMPI–TOFMS mass spectrometry”, Chemosphere **42**, 507–518 (2001).

[10] N. Kjaergaard, L. Hornekaer, A. Thommesen, et al., “Isotope selective loading of an ion trap using resonance-enhanced two-photon ionization”, Applied Physics B **71**, 207–210 (2000).

[11] C. D. Bruzewicz, J. Chiaverini, R. McConnell, et al., “Trapped-ion quantum computing: progress and challenges”, Applied Physics Reviews **6**, 021314 (2019).

[12] B. E. King, C. S. Wood, C. J. Myatt, et al., “Cooling the collective motion of trapped ions to initialize a quantum register”, Physical Review Letters **81**, 1525–1528 (1998).

[13] P. Obšil, A. Lešundák, T. Pham, et al., “Multipath interference from large trapped ion chains”, New Journal of Physics **21**, 093039 (2019).

[14] G. W. Drake and Z. C. Yan, “High-precision spectroscopy as a test of quantum electrodynamics in light atomic systems”, Canadian Journal of Physics **86**, 45–54 (2008).

[15] J. P. Covey, A. Sipahigil, S. Szoke, et al., “Telecom-band quantum optics with ytterbium atoms and silicon nanophotonics”, Physical Review Applied **11**, 034044 (2019).

[16] E. C. Cook, A. D. Vira, C. Patterson, et al., “Testing quantum electrodynamics in the lowest singlet state of neutral beryllium-9”, Physical Review Letters **121**, 053001 (2018).

[17] G. Higgins, W. Li, F. Pokorny, et al., “Single strontium Rydberg ion confined in a Paul trap”, Physical Review X **7**, 021038 (2017).

[18] H. C. Nägerl, C. Roos, D. Leibfried, et al., “Investigating a qubit candidate: Spectroscopy on the $S_{1/2}$ to $D_{5/2}$ transition of a trapped calcium ion in a linear Paul trap”, Physical Review A **61**, 023405 (2000).

[19] S. T. Gulde, “Experimental realization of quantum gates and the Deutsch-Jozsa algorithm with trapped calcium ions”, PhD thesis (University of Innsbruck, 2003).

[20] C. Roos, “Controlling the quantum state of trapped ions”, PhD thesis (University of Innsbruck, 2000).

[21] W. Neuhauser, M. Hohenstatt, P. E. Toschek, et al., “Localized visible $Ba^+$ mono-ion oscillator”, Physical Review A **22**, 1137–1140 (1980).

[22] C. Auchter, T. W. Noel, M. R. Hoffman, et al., “Measurement of the branching fractions and lifetime of the $5D_{5/2}$ level of $Ba^+$”, Physical Review A **90**, 060501 (2014).

[23] F. A. An, A. Ransford, A. Schaffer, et al., “High fidelity state preparation and measurement of ion hyperfine qubits with $I > 1/2$”, Physical Review Letters **129**, 130501 (2022).

[24] B. M. White, P. J. Low, Y. De Sereville, et al., “Isotope-selective laser ablation ion-trap loading of $^{137}Ba^+$ using a BaCl 2 target”, Physical Review A **108**, 039901 (2023).

[25] G. Audi, O. Bersillon, J. Blachot, et al., “The NUBASE evaluation of nuclear and decay properties”, Nuclear Physics A **729**, 3–128 (2003).

[26] D. Lucas, A. Ramos, J. Home, et al., “Isotope-selective photoionization for calcium ion trapping”, Physical Review A **69**, 012711 (2004).

[27] N. Kjaergaard, L. Hornekaer, A. Thommesen, et al., “Isotope selective loading of an ion trap using resonance-enhanced two-photon ionization”, Applied Physics B **71**, 207–210 (2000).

[28] G. Vrijsen, Y. Aikyo, R. F. Spivey, et al., “Efficient isotope-selective pulsed laser ablation loading of $^{174}Yb^+$ ions in a surface electrode trap”, Optics Express **27**, 33907 (2019).

[29] S. Gulde, D. Rotter, P. Barton, et al., “Simple and efficient photo-ionization loading of ions for precision ion-trapping experiments”, Applied Physics B **73**, 861–863 (2001).

[30] K. Yamada, N. Ozaki, M. Yamamoto, et al., “Separation of barium isotopes by selective two-step photoionization process”, Journal of Nuclear Science and Technology **25**, 641–648 (1988).

[31] D. J. Armstrong and J. Cooper, “Isotope-selective photoionization spectroscopy of barium”, Physical Review A **47**, R2446–R2449 (1993).

[32] A. V. Steele, L. R. Churchill, P. F. Griffin, et al., “Photoionization and photoelectric loading of barium ion traps”, Physical Review A **75**, 053404 (2007).

[33] D. Rotter, “Quantum feedback and quantum correlation measurements with a single Barium ion”, PhD thesis (University of Innsbruck, 2008).

[34] S. Noda, M. Fujita, and T. Asano, “Spontaneous-emission control by photonic crystals and nanocavities”, Nature Photonics **1**, 449–458 (2007).

[35] K. J. Russell, T.-L. Liu, S. Cui, et al., “Large spontaneous emission enhancement in plasmonic nanocavities”, Nature Photonics **6**, 459–462 (2012).

[36] A. González-Tudela and D. Porras, “Mesoscopic entanglement induced by spontaneous emission in solid-state quantum optics”, Physical Review Letters **110**, 080502 (2013).

[37] D. B. Higginbottom, “Atom-light couplers with one, two and ten billion atoms”, PhD thesis (The Australian National University (Australia), University of Innsbruck, 2019).

[38] Y. Weiser, T. Faorlin, L. Panzl, et al., “Back action suppression for levitated dipolar scatterers”, Physical Review A **111**, 013503 (2025).

[39] K. J. Arnold, S. R. Chanu, R. Kaewuam, et al., “Measurements of the branching ratios for $6P_{1/2}$ decays in $^{138}Ba^{+}$”, Physical Review A **100**, 032503 (2019).

[40] B. Lauritzen, S. R. Hastings-Simon, H. De Riedmatten, et al., “State preparation by optical pumping in erbium-doped solids using stimulated emission and spin mixing”, Physical Review A **78**, 043402 (2008).

[41] P. Kobel, M. Breyer, and M. Köhl, “Deterministic spin-photon entanglement from a trapped ion in a fiber Fabry–Perot cavity”, npj Quantum Information **7**, 6 (2021).

[42] G. Werth, V. N. Gheorghe, and F. G. Major, *Charged particle traps II: Applications*, Vol. 54, Springer Series on Atomic, Optical, and Plasma Physics (Springer Berlin Heidelberg, Berlin, Heidelberg, 2009).

[43] L. Ruby, “Applications of the mathieu equation”, American Journal of Physics **64**, 39–44 (1996).

[44] G. Araneda, “Experiments with single photons emitted by single atoms”, PhD thesis (University of Innsbruck, 2019).

[45] G. Araneda, G. Cerchiari, D. B. Higginbottom, et al., “The Panopticon device: An integrated Paul-trap-hemispherical mirror system for quantum optics”, Review of Scientific Instruments **91**, 113201 (2020).

[46] B. Brandstätter, A. McClung, K. Schüppert, et al., “Integrated fiber-mirror ion trap for strong ion-cavity coupling”, Review of Scientific Instruments **84**, 123104 (2013).

[47] M. Teller, D. A. Fioretto, P. C. Holz, et al., “Heating of a trapped ion induced by dielectric materials”, Physical Review Letters **126**, 230505 (2021).

[48] D. Leibfried, “Experiments towards quantum information with trapped Calcium ions”, in Aip conference proceedings, Vol. 551 (2001), pp. 130–142.

[49] T. Monz, D. Nigg, E. A. Martinez, et al., “Realization of a scalable Shor algorithm”, Science, 1068–1070 (2016).

[50] B. P. Lanyon, C. Hempel, D. Nigg, et al., “Universal digital quantum simulation with trapped ions”, Science **334**, 57–61 (2011).

[51] F. Schmidt-Kaler, H. Nagerl, H. Rohde, et al., “Crystal structures of Calcium ions for quantum information”, in Technical digest. 1998 eqec. european quantum electronics conference (cat. no.98th8326) (1998), pp. 100–100.

[52] H. Oberst, “Resonance fluorescence of single Barium ions”, diploma thesis (Universität Innsbruck, 1999).

[53] C. Raab, J. Bolle, H. Oberst, et al., “Diode laser spectrometer at 493 nm for single trapped $Ba^{+}$ ions”, Applied Physics B: Lasers and Optics **67**, 683–688 (1998).

[54] A. Kramida, Y. Ralchenko, J. Reader, et al., *NIST Atomic Spectra Database (ver. 5.11)*, Online. Available: `https://physics.nist.gov/asd` [2024, November 6], 2023.

[55] L. Slodička, “Single ion-single photon interactions in free space”, PhD thesis (University of Innsbruck, 2013).

[56] D. A. Steck, *Quantum and atom optics*, Online. Available: `http://steck.us/teaching` [2025, August 18], 2025.

[57] W. A. V. Wijngaarden and J. Li, “Hyperfine splittings and isotope shifts of (6s) $2^1S_0$→(6s6p) $^1P_1$ transition in barium”, Canadian Journal of Physics **73**, 484–488 (1995).

[58] L. Mandel and E. Wolf, *Optical coherence and quantum optics* (Cambridge University Press, Cambridge; New York, 1995).

[59] M. Schubert, I. Siemers, R. Blatt, et al., “Transient internal dynamics of a multilevel ion”, Physical Review A **52**, 2994–3006 (1995).

[60] G. Sebastian, “Quantum correlation experiments with resonance fluorescence photons of single barium ions”, PhD thesis (University of Innsbruck, 2010).

[61] M. Riebe, K. Kim, P. Schindler, et al., “Process tomography of ion trap quantum gates”, Physical Review Letters **97**, 220407 (2006).

[62] D. Rotter, “Photoionisation von kalzium”, diploma thesis (University of Innsbruck, 2003).

[63] J. Choi, E. Lee, D. Yum, et al., “Direct measurement of isotope shifts in the barium $6s^2$ $^1S_0$ - 5d6p $^3D^0_1$ transition”, Physical Review A **110**, 032812 (2024).

[64] J. P. Joule, “On the production of heat by voltaic electricity”, Abstracts of the Papers Printed in the Philosophical Transactions of the Royal Society of London **4**, 280–282 (1843).

[65] G. Leschhorn, T. Hasegawa, and T. Schaetz, “Efficient photo-ionization for barium ion trapping using a dipole-allowed resonant two-photon transition”, Applied Physics B **108**, 159–165 (2012).

[66] M. Mhareb, M. Alqahtani, F. Alshahri, et al., “The impact of barium oxide on physical, structural, optical, and shielding features of sodium zinc borate glass”, Journal of Non-Crystalline Solids **541**, 120090 (2020).

[67] Z. Zhang, K. J. Arnold, S. R. Chanu, et al., “Branching fractions for $P_{3/2}$ decays in $Ba^+$”, Physical Review A **101**, 062515 (2020).

[68] N. V. Vitanov, A. A. Rangelov, B. W. Shore, et al., “Stimulated Raman adiabatic passage in physics, chemistry, and beyond”, Reviews of Modern Physics **89**, 015006 (2017).

[69] J. Johansson, P. Nation, and F. Nori, “QuTiP 2: A Python framework for the dynamics of open quantum systems”, Computer Physics Communications **184**, 1234–1240 (2013).

[70] M. H. Goerz, D. Basilewitsch, F. Gago-Encinas, et al., “Krotov: A Python implementation of Krotov’s method for quantum optimal control”, SciPost Physics **7**, 080 (2019).

[71] R. H. Brown and R. Q. Twiss, “Correlation between photons in two coherent beams of light”, Nature **177**, 27–29 (1956).

[72] P. Hidnert and H. Krider, “Thermal expansion of aluminum and some aluminum alloys”, Journal of Research of the National Bureau of Standards **48**, 209 (1952).

[73] S. Krämer, D. Plankensteiner, L. Ostermann, et al., “Quantumoptics. jl: A Julia framework for simulating open quantum systems”, Computer Physics Communications **227**, 109–116 (2018).

# Danksagung

Zum Abschluss meiner Arbeit möchte ich die Gelegenheit nutzen, mich bei all den Menschen zu bedanken, die mich während meines Studiums unterstützt, motiviert und ausgehalten haben.
Zunächst gilt mein größter Dank Giovanni Cerchiari, der mich stets gefördert, geleitet und unterstützt hat. Ebenso möchte ich mich bei der gesamten Arbeitsgruppe sowie meinen Laborpartnern Yannick Weiser, Tommaso Faorlin und Lorenz Panzl bedanken. Dank euch habe ich mich von Anfang an willkommen und respektiert gefühlt und mich jeden Tag auf die Arbeit im Labor gefreut. Ein besonderer Dank gebührt Yannick, der mich erst dazu überredet hat, meine Masterarbeit im Barium-Team zu schreiben, nur um danach täglich eine Vielzahl an Fragen beantworten zu dürfen. Des Weiteren danke ich Prof. Rainer Blatt und Thomas Monz für die Möglichkeit, meine Masterarbeit in der Quantenoptik-Gruppe durchführen zu können.
Auch die Freundschaften, die vor, während und durch das Studium entstanden sind, sollen hier nicht unerwähnt bleiben. Danke vor allem an Isabella Weisleitner, die mich seit Jahren in all meinen Vorhaben unterstützt und antreibt. Danke, Stefan Kremminger, dass du durch unsere tiefgehenden und faszinierenden Gespräche über das Universum meine Leidenschaft für Physik immer wieder neu entfacht hast. Ein großes Dankeschön auch an Florian Heim, Tobias Zauner und Moritz Hirsch für die willkommene Ablenkung vom Studium – sei es durch spannende Yu-Gi-Oh!-Duelle, entspannte Wanderausflüge, lustige Spieleabende, großartige Konzerte oder intensive Klettersessions. Danke an Julian Gasteiger und Manuel Untergasser für die gemeinsame Zeit in der WG mit entspannten Abenden beim Kochen, Fernsehen und Abschalten. Danke auch an Julian Mitterstieler, der sich immer wieder für meine Arbeit im Labor interessiert und mich so zusätzlich motiviert hat.
Ein besonderer Dank geht auch an Florian Kofler, Rene Nardi und Elyas Mattivi, die mich besonders während meiner Masterarbeit durch spannende Dungeons & Dragons-Sessions nach der Arbeit entspannen ließen. Danke an Leo Walz für die anregenden Gespräche im Büro. Ebenso danke ich allen, die mit mir im Physikstudium gelernt und gelitten haben - besonders Lena Tokuhiro und Jutta Schnizer für die langen Abende beim Protokollschreiben und PS-Aufgaben lösen.
Zu guter Letzt möchte ich meiner Familie danken – allen voran Mama, Papa, Jotti und Babsi - für ihre bedingungslose Unterstützung in allem, was ich tue.

## Verwendung von KI basierten Werkzeugen

Ich erkläre hiermit, dass ich KI basierte Werkzeuge ausschließlich zur sprachlichen Unterstützung, insbesondere zur Grammatikprüfung, Übersetzung und stilistischen Überarbeitung, verwendet habe. Der wissenschaftliche Inhalt, die Analysen, Interpretationen sowie die Schlussfolgerungen dieser Arbeit stammen vollständig von mir.